Turbulent and Boundary Layer Characteristics during VOCALS-REx

Dillon S. Dodson[1] and Jennifer D. Small Griswold[1]

[1]Department of Atmospheric Sciences, University of Hawaii, Manoa, Honolulu, HI, USA

Correspondence: Jennifer D. Small Griswold (smalljen@hawaii.edu)

Abstract.

Stratocumulus clouds have a significant impact on climate due to their large spatial extent, with areas of enhanced coverage termed stratocumulus decks. How turbulence evolves with time and influences the stratocumulus deck properties however, in particular throughout the vertical profile of the boundary layer, is still lacking through model parameterizations of the small-scale flow. Collecting in situ data to better understand the turbulence and physical processes occuring within the stratocumulus deck therefore key to better model parameterizations. Boundary layer and turbulent characteristics, along with synoptic scale changes in these properties over time, are examined using data collected from 14 research flights made with the CIRPAS Twin Otter Aircraft. Data was collected during the VOMOS Ocean-Cloud-Atmosphere-Land Study-Regional Experiment (VOCALS-REx) at Point Alpha in October and November of 2008 off the cost of South America ($20°$S, $72°$W).

Findings show that the influence of a synoptic system on Nov 1st and 2nd brings in a moist layer above the boundary layer, leading to a deepening cloud layer and precipitation during passage, and a large increase in boundary layer height and cloud thinning after passage. The maximum value in turbulent kinetic energy (TKE) was measured on Nov. 1st due to precipitation destabilizing the sub-cloud layer while a minimum occurred on Nov. 2nd after precipitation had ceased due to turbulent mixing overturning the boundary layer and depleting the initial turbulent energy produced from the evaporation of precipitation below cloud base. Turbulent properties averaged over all 14 flights reach a maximum near cloud middle (between normalized in-cloud values of 0.25-0.75), with well mixed boundary layers experiencing two peaks in TKE, one near cloud base due to latent heat release and another near cloud top due to evaporational cooling. Overall, it appears that turbulence measured at Point Alpha is weaker than that measured over the open ocean to the west of Point Alpha, and that measured during other scientific campaigns. Synoptic scale analysis suggests that as the geopotential height decreases, the boundary layer height and entrainment zone thickness increases, accompanied by a decrease of in-cloud and below-cloud turbulence, and vice versa.

1 Introduction

Stratocumulus (Sc) clouds have a significant impact on climate due to their large spatial extent, covering approximately 20% of Earth's surface (23% over the ocean and 12% over the land) in the annual mean (Randall et al., 1984). According to Wood (2012), the subtropical eastern oceans in particular are marked by extensive regions of Sc sheets (often referred to as semipermanent subtropical marine stratocumulus sheets). Of those, the largest and most persistent Sc deck in the world, the Peruvian Sc deck, lies off the west coast of South America (Bretherton et al., 2004), making its role in climate an essential building block to better modeling the overall earth system. A better understanding of not only the Peruvian Sc deck, but all Sc decks, is therefore necessary to make advancements in modeling and representing the present-day and future climate system.

It is a challenge for models to successfully simulate the Peruvian Sc deck due to the importance of subgrid scales and physical processes which are poorly represented (Wood et al., 2011). In particular, most models continue to struggle with the boundary layer vertical structure (Wyant et al., 2010) which is important for determining Sc cloud properties. For example, vertical profiles of turbulent fluxes (liquid water, water vapor, energy) determine the mean state of the boundary layer and the resulting properties of the Sc deck (Schubert et al., 1979; Bretherton and Wyant, 1997).

Although turbulence is critical to atmospheric boundary layer, microphysical, and large scale cloud dynamics, it is difficult to measure. One of the major research problems of cloud microphysics remains in being able to understand the fundamental importance of turbulent processes occurring on extremely small scales, along with gathering in situ data to better understand these turbulent properties (Shaw, 2003). This study therefore aims to characterize turbulence throughout the vertical profile of the Stratocumulus topped marine boundary layer (STBL) over a three-week observation period in October and November of 2008 during the Variability of the American Monsoon Systems (VAMOS) Ocean-Cloud-Atmosphere-Land Study-Regional Experiment (VOCALS-REx). A large in situ dataset was collected throughout the boundary layer, allowing for analysis (on a variety of spatial and temporal scales) in the aims of improving predictions of the Southeast Pacific coupled ocean-atmosphere-land system (Wood et al., 2011). This dataset allows for a classification of turbulent properties not only through vertical profiles, but provides an opportunity to analyze how turbulence changes within the boundary layer with varying synoptic conditions.

The main objectives of this paper include a quantification of the levels of turbulence occurring within the boundary layer through the evaluation of turbulent kinetic energy dissipation rates and other turbulent measurements. In particular, the main goals include: (1) Determine average turbulent values throughout the vertical structure of the STBL, classifying the STBL based on different turbulent profiles analyzed; (2) Analyze day to day variability in turbulent measurements and boundary layer characteristics, relating them to synoptic changes in meteorological conditions. Although papers analyzing the overall characteristics of the boundary layer during VOCALS-REx exist (i.e., Zheng et al. (2011)), an extensive look at turbulent properties has yet to be published. A general lack of information on turbulent properties and synoptic scale changes in mean atmospheric conditions is lacking, in particular for marine boundary layers. Analysis of turbulence with changes in synoptic conditions and frontal passages is abundant for locations on land however (i.e., Young and Johnson (1984); Shapiro et al. (1985); Taylor et al. (1993); Frank (1994); Chapman and Browning (2001)). Section 1.1 introduces typical boundary layer vertical structure. Section 2 provides an overview of the data and methods, followed by synoptic and boundary layer charac-

teristics during VOCALS-REx in Section 3. Section 4 will evaluate and discuss the results. Section 5 will provide concluding remarks.

1.1 Boundary Layer Vertical Structure

The vertical structure of the boundary layer is strongly tied to the horizontal and vertical structure of Sc clouds (Lilly, 1968;

60 Bretherton et al., 2010). The STBL is characterized by Sc cloud tops located at the base of an inversion, with subsiding air aloft (as part of the descending branch of the Hadley cell circulation) and well mixed conditions and near-constant conserved variables with height throughout the boundary layer (Wood, 2012). Multiple papers have analyzed typical well mixed STBL vertical structures (i.e., Albrecht et al. (1988); Nicholls (1984)), showing constant potential temperature and mixing ratio with height up until the inversion, when the mixing ratio (potential temperature) sharply decreases (increases). Horizontal winds

65 (both direction and velocity) are typically constant with height throughout the well mixed boundary layer, with changes in both direction and strength typically present at the top of the STBL, influencing cloud-top mixing (Wood, 2012).

Convection in the STBL is limited. Unlike updrafts through convective heating over the ground, updrafts within the STBL do not penetrate the inversion. This is because convection within the STBL is primarily driven by longwave radiational cooling at cloud top and not heating at the ocean surface. The longwave radiation cools the cloud top, leading to instability and the

70 convection of warmer, moist air at the surface (Lilly 1968). The cloud cover is greatest when the STBL is shallow [$0.5 < z_i$ < 1 km], where z_i is the boundary layer height (Wood and Hartmann, 2006). It is known that clouds are areas of enhanced turbulence (Pinsky and Khain, 1996). Therefore, Sc sheets are turbulent but in contact with an almost non-turbulent upper atmospheric environment. This results in the entrainment of the upper (laminar flow) layer into the lower (turbulent flow) layer. Through the entrainment of free tropospheric air as just described, the STBL deepens beyond 1-km and becomes decoupled.

75 According to Bretherton and Wyant (1997), due to longwave cooling at the cloud top being unable to maintain mixing of the positively buoyant entrained air over the entire depth of the STBL, the upper (cloud containing) layer becomes decoupled from the surface moisture supply. This process leads to a transition from Sc to cumulus clouds (leading to a subsequent reduction in cloud cover) over the subtropical oceans.

The vertical profile of various turbulent fluxes, particularly that of buoyancy, can tell one a lot about the state of the STBL. For

80 a boundary layer to remain well mixed, the vertical energy and moisture fluxes must be linear functions of height. According to Bretherton and Wyant (1997), the buoyancy flux is not a linear function of height however (unlike that of a dry boundary layer). An increase in the buoyancy flux above the lifted condensation level (LCL) is typically proportional to the upward transport of liquid water that is required to sustain the cloud against entrainment drying (i.e., mixing is sustained by surface fluxes). Decoupling of the boundary layer (and the subsequent decrease in cloud cover) can occur when the subcloud buoyancy

85 fluxes become negative, inhibiting convection below cloud base (Albrecht et al., 1988). According to Shaw (2003), one of the main sources of turbulent kinetic energy (TKE) in clouds is evaporative cooling (due to the entrainment of dry air) and condensational heating (due to droplet condensational growth), implying the buoyancy flux is the primary generator of TKE in the STBL (Schubert et al., 1979). Given this, the buoyancy flux nearly always has a maximum in the cloud layer (Nicholls and Leighton, 1986; Bretherton and Wyant, 1997), with TKE being generated due to longwave and evaporational cooling at cloud

90 top, and condensational heating at cloud base (Moeng et al., 1992). Nicholls (1989) observed through aircraft observations that the largest buoyancy fluxes are close to cloud top, with further observations (Caughey et al., 1982; Nicholls, 1989) suggesting that the descending regions of air originating near cloud top are more a result of radiative cooling rather than evaporative cooling.

Vertical velocity variance typically displays the strongest updrafts and downdrafts in the upper half of the STBL (Hignett,
95 1991), consistent with the largest production of turbulence being contained within the cloud layer. A positive (negative) vertical velocity skewness indicates that strong narrow updrafts (downdrafts) are surrounded by larger areas of weaker downdrafts (updrafts). It has been found that negative vertical velocity skewness is typically contained within most of the cloud layer and below (Nicholls and Leighton, 1986; Nicholls, 1989), whereas a decoupled boundary layer containing cumulus below stratocumulus may contain positive vertical velocity skewness (de Roode and Duynkerke, 1996).

100 The main source of moisture for the STBL is supplied by the surface latent heat flux, making it an important source of buoyant TKE production (Bretherton and Wyant, 1997), with the surface sensible heat flux typically being a much weaker source of turbulence. The sensible heat and latent heat flux can be compared using the Bowen ratio (the ratio of the sensible to the latent heat flux). The smaller the Bowen ratio, the more proportional the liquid water flux in the cloud layer is to the upward moisture or latent heat flux. This results in a larger latent heat flux leading to decoupling due to the latent heat flux
105 concentrating convective energy generation (through condensational and evaporational heating/cooling) within the cloud layer. Lewellen et al. (1996) reached a comparable conclusion through assigning shallow stratocumulus layers to preset surface fluxes. This process naturally leads to the buoyancy flux being at a minimum in the sub-cloud layer, priming the boundary layer for decoupling. It is argued in (Bretherton and Wyant, 1997) that the surface latent heat flux is the most important determinant of decoupling within the STBL.

110 2 Data and Methods

2.1 Data

Data was collected during the Variability of the American Monsoons (VAMOS) Ocean Cloud-Atmosphere-Land Study-Regional Experiment (VOCALS-REx) from the Peruvian Stratocumulus deck off the west Coast of Chili and Peru during October and November of 2008. VOCALS-REx used various platforms, including five aircraft and two research vessels to ac-
115 cumulate an extensive dataset of the boundary layer, lower free troposphere, and cloud deck along $20°$S from $70°$W to $85°$W. Although multiple sampling platforms, locations, and mission types were deployed during the campaign (see Wood et al. (2011)), data collected by the Center for Interdisciplinary Remotely-Piloted Aircraft Studies (CIRPAS) Twin Otter aircraft will be the focus of this paper, which collected data in the vicinity of $20°$S, $72°$W; from here on termed Point Alpha. The Twin Otter aircraft was operational for 19 flights from October 16th to November 13th, 2008.

120 The Twin Otter platform is ideal for a turbulent analysis of the boundary layer due to the aircraft being instrumented to make turbulence and cloud microphysics measurements, with the same location being sampled for each flight. The Twin Otter is also a relatively slow-moving aircraft with a flight speed of roughly 60 ms^{-1}, allowing for a higher resolution of spatial

sampling as compared to a faster moving aircraft. Each of the Twin Otter flights was carried out using a stacked flight path (Wood et al., 2011), which involved using stacked legs of 50-100 km in length (horizontal flight paths) to sample various levels

125 of the boundary layer and cloud layer, with at least one aircraft vertical sounding (vertical profile) performed for each flight where the aircraft sampled the free upper troposphere and boundary layer in a single ascent or descent. Each flight of five hours originated from Iquique Chile, allowing for roughly three hours of sampling at Point Alpha.

Of the 19 flights performed by the Twin Otter, only 14 are used here due to instrumentation failure on five of the flights (Phase Doppler Interferometer and the cloud/aerosol probe). Table 1 displays each of the Research Flights (RF) used in this

130 paper. All flights occurred during the day, with all but two flights (RF 8 and RF 17) starting around 7:00 AM local time, with the first vertical profile flown around 8:00 AM local time at Point Alpha. Having each flight sample the same location at roughly the same time is critical, as turbulence typically displays diurnal patterns, with the strongest turbulent mixing occurring during the night when longwave radiational cooling dominates due to the absence of the stabilizing effect of shortwave absorption at cloud top (Hignett, 1991). Meteorological variables were collected at 40-Hz (including u, v, and w wind velocity, wind

135 direction, mixing ratio and potential temperature, to name a few) while most cloud and aerosol data were collected at 1-Hz. A more in-depth description of the instrumentation used and values measured on the Twin Otter can be found in Zheng et al. (2010) and Wood et al. (2011).

To analyze the synoptic conditions over the study period, data from the National Centers for Environmental Prediction (NCEP) / National Center for Atmospheric Research (NCAR) Reanalysis Project (NNRP, Kistler et al. (2001)) will be used.

140 Data resolution of the NCEP/NCAR reanalysis data is 2.5° x 2.5° x 17 pressure levels, available at six hour intervals. The resolution of this data is suitable for analyzing synoptic scale patterns, but is not ideal for depicting mesoscale variability that may be present from day to day.

2.2 Turbulent Calculations

The randomness of turbulence makes deterministic description difficult, limiting description to statistics and average values of

145 turbulence, in particular that of Reynolds decomposition (or averaging). Reynolds decomposition uses a mean value (over some time period) and subtracts it from the actual instantaneous velocity to obtain the turbulent component (or perturbation value). Reynolds decomposition is based on the underlying assumption that the turbulence is isotropic and stationary, conditions that are hardy fulfilled for atmospheric boundary layer flows however, especially when working with data spanning larger timeframes. The problem is defining how to average collected data to best represent the mean and turbulent components for

150 the fluid flow (with shorter subsets of data having more stationary properties in general than that of longer subsets of data). Following the methods outlined in Jen-La Plante et al. (2016), who used a 300-point averaging window, a 320-point averaging window is used here for all turbulent analysis. A 320-point averaging window corresponds to 8 second subsets of data (using 40-Hz data), or a roughly 440-m subset of data in the horizontal spatial scale (assuming average aircraft speed of 55 ms^{-1}). Linear regression is then applied to each 320-point averaging window to calculate the mean value and determine the perturbation

155 values.

Applying the averaging method discussed above leads to the calculation of the fluctuations of the u, v, and w components of the velocity, along with other parameters used to measure various turbulent fluxes. Variables to be obtained include turbulent kinetic energy, which is given by:

$$TKE = \frac{1}{2}\left(\overline{u'^2} + \overline{v'^2} + \overline{w'^2}\right) \tag{1}$$

160 where u', v', and w' are the fluctuations of the velocity components. The turbulent sensible heat, latent heat, and buoyancy fluxes will also be obtained, given by:

$$F_\theta = C_p\bar{\rho}\overline{w'\theta'} \tag{2}$$

$$F_q = L_v\bar{\rho}\overline{w'q'} \tag{3}$$

$$F_{\theta_v} = C_p\bar{\rho}\overline{w'\theta'_v} \tag{4}$$

165 respectively. Where C_p is the specific heat of air (1005 J kg^{-1}K^{-1}), L_v is the latent heat of vaporization at 20°C (2.45 $\cdot$ 10^6 J kg^{-1}), ρ is the mean air density, and θ', q', and θ'_v are the potential temperature, mixing ratio, and virtual potential temperature perturbations, respectively. Note that θ_v is commonly used as a proxy for density when calculating the buoyancy.

Just like that of Reynolds decomposition, the calculation of the TKE dissipation rate (ϵ) is based on conditions that the flow is isotropic (i.e., uniformity in all directions), making the measurement of ϵ challenging. In particular, classical turbulence theory

170 in the inertial subrange from Kolmogorov (1941) is based on assumptions of local isotropy. With that said, there are multiple methods to measure the TKE dissipation rate, including the inertial dissipation method, structure functions, and the direct method. Siebert et al. (2006) found that both the inertial dissipation and structure function methods are useful, but the inertial dissipation method sometimes underestimates ϵ at low values due to no clear inertial subrange behavior being observed in the power spectral density, which is not the case for the structure function. The structure function method is therefore considered

175 more robust for cases with small values of ϵ, and will be used here. Due to questions of isotropy, the TKE dissipation rate will be evaluated on the u, v, and w components of the wind, and an average dissipation rate will be calculated from the three components.

The calculation of the dissipation rate comes from the analysis of the velocity perturbations through nth order structure functions. The perturbations, as for other turbulent parameters, are determined with respect to an averaging window of 320-

180 points. Each subset of perturbations is then appended to the end of the previous subset to create a single time series of velocity perturbations. The structure function is given by:

$$S_n(l) = \left(\overline{|u(x+l)-u(x)|}\right)^n \tag{5}$$

where l is the distance (or in the case of a temporal series, l is equivalent to t assuming constant flight speed). From Frisch (1995), the dissipation rate using the nth order structure function can be obtained by using:

185 $$S_n(l) = C_n|l\epsilon|^{\frac{n}{3}} \tag{6}$$

where C_n is a constant of the order 1. The second order structure function will be used here ($n = 2$), where C_2 is equal to 2 for transverse velocity fluctuations and C_2 is equal to 2.6 for longitudinal velocity fluctuations (Chamecki and Dias, 2004),

where vertical fluctuations are considered transversal and horizontal fluctuations (both u' and v') are considered longitudinal, following the methods in Jen-La Plante et al. (2016). The structure function follows a $-2/3$ power law and will only be
190 used to calculate the dissipation rate between frequencies of 0.3-5-Hz, neglecting the higher frequency features attributed to interactions with the plane and other instrumental artifacts.

3 Synoptic and Boundary Layer Characteristics

3.1 Mean Synoptic Conditions

The Southeast Pacific Ocean is found on the eastern edge of the south-Pacific semipermanent subtropical anticyclone, char-
195 acterized by large scale upper tropospheric subsidence leading to a strong temperature inversion with a well-mixed boundary layer below. The surface pressure therefore is controlled in part by the location of the south-Pacific subtropical anticyclone. This anticyclone is routinely interrupted (especially between fall and spring) by periods of relative low pressure which is associated with localized troughing or the passage of midlatitude cyclones to the south. Several papers (Toniazzo et al., 2011; Rahn and Garreaud, 2010) have analyzed the synoptic characteristics during VOCALS-REx, these papers however tend to focus on
200 the VOCALS-REx region as a whole, and not specifically on Point Alpha, which is done in this section.

Figure 1 shows the mean of large-scale meteorological conditions (including sea level pressure, omega, and 700-hPa geopotential height) from NCEP reanalysis data over the study region between October 19th to November 12th. The mean sea level pressure (panel (a)) displays the anticyclone near it's climatological position of 30°S, 100°W (Toniazzo et al., 2011). The overlaid sea level pressure standard deviation (only displayed up to 20 hPa) shows variability increasing southward, indicating
205 enhanced midlatitude storm tracks. Enhanced variability that is in line with midlatitude troughing from panel (b) also decreases toward the coast, suggesting more variation in the synoptic pattern over the open ocean as compared to the near-coastal region. This is as expected, as Barret et al. (2009) found that synoptic systems tend to weaken as they move towards the coast of South America.

The mean 700-hPa geopotential height is displayed in panel (b), overlaid with omega data. Subsidence (green shading)
210 dominated the VOCALS-REx region, with Point Alpha having an average value of 0.066 Pa s^{-1} at the 700-hPa level. While enhanced storm tracks were primarily contained within the mid-latitudes, the 700-hPa geopotential height displays midlatitude troughing extending between Point Alpha and the subtropical high (as was found in (Zheng et al., 2011), suggesting that meteorological conditions at Point Alpha were influenced by both midlatitude synoptic systems and the subtropical anticyclone.

The sea-level pressure was also measured using both reanalysis data and aircraft 30-m level horizontal flight legs. Figure 2,
215 panel (a) shows that the reanalysis data at Point Alpha tended to be on average 1.5-hPa greater than the aircraft measured sea level pressure. The pressure decreased by roughly 3-hPa from October 19th to November 12th, however, this decrease cannot be considered a seasonal signal because it is within synoptic scale variation. The sea surface temperature (SST) and atmospheric surface temperature (both measured during 30-m horizontal flight legs) increased steadily throughout the observation period, increasing by 2.79 and 2.28 °C, respectively.

3.2 Synoptic Variability at Point Alpha

Synoptic variability at Point Alpha is summarized by time series of geopotential height at various levels. Higher geopotential heights are associated with ridging aloft while decreases in geopotential heights are associated with synoptic disturbances or troughs. The 500-hPa geopotential height (see Figure 2) varied between 5840 and 5900-hPa, with an increase of 9-hPa between October 19th and November 12th. Figure 2 also displays enhanced synoptic scale variation during October, with several disturbances effecting Point Alpha. The 500, 700 (panel (c)), 850, and 1000 (panel (d)) hPa geopotential heights alternate between areas of high and low height through November 2nd. After November 2nd, the 500-hPa geopotential height is more consistent, with height increasing over Point Alpha until November 10th, at which point the height begins to decrease.

Besides minor disturbances in October, there are two main disturbances that stand out. The first disturbance occurs on November 1st and 2nd (green shading in Figure 2), where both the 500 and 700-hPa heights have minimums (5842 and 3134 m, respectively). The 850 and 1000-hPa heights also have secondary minimums. The second disturbance was the formation of a costal low, which can be seen by decreasing geopotential heights on November 12th. Both the 850 and 1000-hPa geopotential heights reached minimums on November 12th (1498 and 104 m, respectively). This costal low reached a minimum (the coastal low was strongest) after the analysis period, on November 15th (Rahn and Garreaud, 2010). The ridging which formed after November 2nd leads to the formation of the coastal low through the warming of the lower and middle troposphere (Garreaud and Rutllant, 2003).

How the boundary layer turbulence changed with the synoptic evolution, particularly the disturbance observed on November 1st and 2nd, will be the focus of this paper. The 700-hPa geopotential height map displayed a midlatitude trough developing and extending past Point Alpha from October 29th through November 3rd, as is shown in Figure 3. A deep midlatitude trough forms off the west coast of South America by October 30th, extending past 15°S. The trough axis begins to move over Point Alpha by October 31st, with the main impacts of the trough on Point Alpha (in terms of lowest geopotential height) being observed on November 1st and 2nd. The 500-hPa geopotential height map (not shown here) shows the ridge axis directly over Point Alpha on November 1st.

Figure 4 (panels (a) through (c)) show atmospheric wind direction and velocity using data collected from horizontal flight legs. Panel (d) displays wind direction using data collected from aircraft vertical soundings. Atmospheric winds near the surface (measured during 30-m horizontal flight legs) at Point Alpha were mostly southerly (150 to 180°) with a mean of 176°. Strong wind shear was present near the inversion, with winds above the marine boundary layer (measured during horizontal flight legs above the inversion) having a mostly northwesterly component (mean of 273°) while having more variability in direction than that of the boundary layer (300 to 360°). Although on most flight days the winds speed and direction were mostly constant with height in the boundary layer (see panel (d)), on November 1st and 4th (blue lines) the wind direction shifted sharply within the boundary layer from southerly to northeasterly. On November 2nd (green line), the wind direction had its strongest westerly component (214°). Shear within the boundary layer is not common. Zheng et al. (2011) suggest that this shear is linked to coastal processes such as the propagation of the upsidence wave. It should also be noted however that the wind shear within the boundary layer is present on the same day (November 1st) that the trough axis is located over point alpha. On the

proceeding day, the surface winds experience their most westerly component. According to Rahn and Garreaud (2010), as

255 troughs approach the coast of South America, southeast winds are typically replaced by southwest winds. Between October 29th and November 2nd, wind direction within the boundary layer shows its most variation, gradually shifting from $153°$ (most easterly component measured) to $213°$ (most westerly component measured), respectively. While the trough approaches the coast of Chile, southeast winds are replaced by southwest winds, as is typical of synoptic scale disturbances (Rahn and Garreaud, 2010).

260 **3.3   Boundary Layer Characteristics**

Boundary layer height is perhaps the most important feature of the marine boundary layer (MBL), with the height being one of the main dictators for boundary layer characteristics such as decoupling and cloud cover (Albrecht et al., 1995). Findings from Rahn and Garreaud (2010) at a separate observation point within the VOCALS-REx region suggests that the boundary layer depth tended to be either low (600-m) or high (1500-m) with periods of high or low depth interrupted by rapid transitions

265 between the two states over 12 to 36 hour periods due to synoptic variability. Figure 5 shows the thickness of the Sc cloud layer, the thickness of the inversion (entrainment zone), and subsequently the MBL height for each flight. The cloud layer was identified using a liquid water content (LWC) greater than or equal to 0.01 g m^{-3}, while the inversion layer was identified by the region of greatest change in the mixing ratio (change $\geq$ |0.10 g kg^{-1}| per measurement) and potential temperature (change $\geq$ |0.20 K| per measurement) within the vertical profiles. This results in the bottom of the inversion layer characterized by the

270 profiles beginning to lose the boundary layer features, while the top of the inversion layer had lost all boundary layer features.

The average height of the boundary layer was 1175-m (see Table 2 for boundary layer characteristics), with the average cloud layer and inversion thickness being 239 and 59-m, respectively. The sharp inversion layer suggests that the interaction between boundary layer and free tropospheric air aloft extended over a relatively thin layer. Figure 5 shows that the boundary layer height varied between 996 and 1450-m, with mostly gradual changes in height from flight day to flight day. The average

275 change in boundary layer height was 68 m day^{-1} with four occurrences of a rate of change above 100 m day^{-1}. After October 27th is when the most significant changes took place to the cloud thickness and boundary layer height. Between October 27th and 29th (no flight day in-between), the boundary layer height increased from 995 to 1300-m (152 m day^{-1}, the second largest rate of change). The next four flight days recorded the thickest cloud layers, peaking on November 1st and 2nd with thicknesses of 382 and 472-m, respectively. It should also be noted that between October 29th and 30th, the boundary layer

280 height decreased from 1300 to 1177-m (124 m day^{-1}, the third largest rate of change). After November 2nd, the cloud layer thins and the boundary layer height increased from 1136-m to 1450-m between November 4th and November 8th. Although this is a rate of 79 m day^{-1}, there is no in situ data in-between November 4th and 8th. It is unknown whether the boundary layer height increased rapidly over a day or two (as would be expected from findings in Rahn and Garreaud (2010)), or gradually increased day over day in-between flights. After the boundary layer height peaks on November 8th, the boundary layer height

285 falls rapidly over the next two days, showing decreases of 174 m day^{-1}and 102 m day^{-1} from November 8th to November 10th.

Although the time series of cloud droplet number concentration is not shown here, it showed a notable dip to a minimum on November 1st of 81 cm^{-3} (where the average is 292 cm^{-3}), corresponding with minimums in both boundary layer cloud condensation nuclei and aerosol number concentration. Above boundary layer aerosol number concentration both had a max-
290 imum on November 1st however. This can most likely be attributed to enhanced moisture (see Figure 6) above the boundary layer due to the passing synoptic system. Figure 6 shows vertical profiles (based on a normalized boundary layer height) of potential temperature, mixing ratio, liquid water content, and the aerosol number concentration. Individual flight profiles are in gray, with the red profile representing the mean and the blue profiles representing the flights conducted on November 1st (RF11) and November 2nd (RF12). Mean profiles show that on average the MBL is well mixed up to the inversion, which
295 then prevents mixing into the free atmosphere above (as evident by the decrease in aerosol number concentration between the boundary layer and free atmosphere above).

The largest deviations from the mean in the profiles occur during the passage of the synoptic system on November 1st and 2nd. At this time, both RF11 and RF12 measured (1) The thickest Sc cloud layer, with November 1st having the largest average cloud droplet size (20.8 μm) and in-cloud drizzle rates, while November 2nd had the lowest recorded cloud base and largest
300 recorded liquid water content; (2) The largest mixing ratio above the boundary layer. This suggests the presence of a moist layer aloft which may have helped in producing the thickest cloud layers observed; (3) The smallest differences in both potential temperature and mixing ratio from the bottom to the top of the inversion layer. During the passage of strong events as described by Rahn and Garreaud (2010), the inversion defining the MBL erodes, making it hard to define the boundary layer height. This process is partially displayed by the small differences in temperature and moisture across the inversion layer during the passage
305 of the synoptic disturbance.

The differences in mixing ratio and potential temperature can be better visualized in Figure 7, which shows the differences between below and above inversion values in panel (b). Data between normalized boundary layer height values of 0.85 and 0.95 were used for the averages below the inversion, while data between normalized altitude values of 1.10 and 1.20 were used for the averages above the inversion. Besides November 1st, 2nd, and to a lesser degree November 4th, the average difference
310 in potential temperature across the inversion was 17-K, while the average difference in mixing ratio was -6.2 g kg^{-1}. On November 1st when both reached a minimum, the difference between the mixing ratio and potential temperature across the inversion was 1.9 g kg^{-1} and 14-K, respectively.

Analyzing wheather the boundary layer is well mixed or not (as displayed in Table 1) based on potential temperature and mixing ratio can be quantified using the decoupling parameters α_θ and α_q, respectively (Wood and Bretherton, 2004). The
315 decoupling parameters measure the relative difference in mixing ratio and potential temperature between the bottom (near the surface) and top (near the inversion) portions of the boundary layer, and are given by

$$\alpha_\theta = \frac{\theta(z_i^-) - \theta(0)}{\theta(z_i^+) - \theta(0)} \tag{7}$$

$$\alpha_q = \frac{q_t(z_i^-) - q_t(0)}{q_t(z_i^+) - q_t(0)} \tag{8}$$

where z_i^+ (z_i^-) is the level $\sim$25 m above (below) the inversion, and $\theta(0)$ and $q_t(0)$ are the potential temperature and mixing ratio at the surface. Here, z_i^+ is calculated using data between normalized boundary layer heights of 1.03 to 1.05, while z_i^- is calculated using data between normalized boundary layer heights of 0.95 to 0.97 (this is roughly 25 m above and below the inversion). The closer to zero the decoupling parameters are, the more well-mixed the boundary layer is. Previous observations suggest that if the parameters exceed ~ 0.30, the boundary layer is decoupled (Albrecht et al., 1995).

Figure 7 shows the decoupling parameters in panel (a). The average value of α_θ (α_q) is 0.15 (0.07), both which are within the regime of well mixed. During RF11 and RF12 the mixing ratio increases above the inversion leading to large values for α_q, while the potential temperature change is relatively small as compared to other flights, with α_θ being above 0.30 during November 1st. Zheng et al. (2011) suggest drizzle processes act to stabilize the boundary layer, leading to decoupling on November 1st. Although on November 8th both parameters are below 0.30, the boundary layer is decoupled due to the presence of a secondary cloud layer below the Sc deck that is visible from analyzing the LWC profiles.

4   Results

The vertical variation in turbulent properties and fluxes can be conveniently discussed in terms of dividing the boundary layer into vertical layers. Here, we will quantify the amount of turbulence occurring within the boundary layer. In particular, analysis includes: (1) Determine average turbulent values throughout the vertical structure of the STBL, classifying the STBL based on different turbulent profiles analyzed; (2) Analyze day to day variability in turbulent measurements and boundary layer characteristics, relating them to synoptic changes in meteorological conditions. For each flight analyzed here, the Sc deck lies directly below a strong inversion. This extreme vertical gradient can cause instrument response issues with the measurement of both the dry bulb and dew point temperature for some distance beneath cloud top (Nicholls and Leighton, 1986). Therefore, data collected during both vertical profiles and horizontal legs will be used and compared.

4.1   Synoptic Variability of Turbulence

Figure 8 shows the mean surface (30-m horizontal flight leg) latent heat flux (panel (a)), sensible heat flux (panel (b)), and Bowen ratio (panel (c)) for each flight day with the standard deviation represented by the gray envelope. Note that for days with two or more mean values, there were two or more 30-m horizontal flight legs, with good agreement between mean leg values within the same flight. The latent heat flux peaks on Oct 26th with a value of 53.3 W m^{-2}, and from that point decreases steadily to its minimum values of 19.7 and 18.5 W m^{-2} just as and after the minimum in geopotential height on Nov. 2nd and 4th, respectively. The sensible heat flux has a sharp increase to its maximum value of 17.1 W m^{-2} on Nov 1st and decreases to its secondary minimum on Nov. 2nd (note that mean values of surface fluxes can be found in Table 3). The Bowen ratio is typically small (less than 0.20), especially for the first half of the campaign. The Bowen ratio has a sharp increase on Nov 1st to match the increase in the latent heat flux (and remains above 0.20 for the remainder of the analysis period), suggesting that the liquid water flux in the cloud layer should not be taken to be proportional to the upward latent heat flux after Nov 1st.

350   Figure 9 gives the surface friction velocity (vertical transport of horizontal momentum), vertical velocity variance, TKE, and the TKE dissipation rate in Panels (a) through (d), respectively. One commonality between each parameter is that the maximum value is reached on Nov. 1st followed by the minimum value on Nov. 2nd (see Table 3 for the mean and range of the values). For all four variables, there is very little variation between measurements, except for between Oct 30th and Nov 2nd, where a large increase in turbulence is observed before a rapid decrease. Overall, there is good agreement between mean values for

355   the same flight, with the exception of Nov 12th, which contains the largest difference between mean values for each variable in discussion here. This large difference was not observed however for the surface latent and sensible heat flux. Note that the average surface values of latent and sensible heat are generally in agreement with those found in Zheng et al. (2011), who found values of 48.5 and 7.1 W m^{-2}, respectively. The differences most likely arise due to different averaging techniques.

    Shifting focus to the entire depth of the boundary layer, Figure 10 shows boxplots (made up of leg mean values) of below-

360   cloud (white) and in-cloud (blue) values of latent heat flux (Panel (a)) and buoyancy flux (Panel ((c)). Panels (b) and (d) display histograms of the latent heat flux and buoyancy flux data with normal distribution fits for reference, respectively. The overall latent heat flux was 11.03 ± 12.97 Wm^{-2}, with the below-cloud mean being 15.74 ± 16.4 Wm^{-2} and the in-cloud mean being 6.01 ± 3.75 Wm^{-2}. The below-cloud latent heat flux is clearly offset to larger values, owing to surface evaporation and subsequent transport of moisture. The red dots in Panel (a) represent the surface values, which are always the largest within the

365   entirety of the vertical layer. The lowest mean values occurred on the same days as the minimum in geopotential height, Nov 1st and 2nd, with values of 5.51 and 4.67 Wm^{-2}, respectively. Although these two data sets are visually different, statistically speaking they are similar, with a p-value of 0.22 (note that all statistical significance testing will be carried out using the Wilcoxon-Sum-Rank-Test).

    The buoyancy flux in Panel (c) displays that the overall mean buoyancy flux was 4.89 ± 4.86 Wm^{-2}, with the below cloud

370   mean being 4.64 ± 3.94 Wm^{-2} and the in-cloud being 5.12 ± 5.64 Wm^{-2}. From just analyzing the mean values of flight legs, there does not appear to be a large difference in the buoyancy flux between the below cloud and in-cloud sections of the boundary layer, which is not as expected. In-cloud buoyancy in general is enhanced due to latent heating and cooling effects. There is no statistical significance between the in-cloud and below-cloud data, with a p-value of 0.39. While the medians in the data populations are similar, the buoyancy flux in-cloud has a much larger range, suggesting isolated occurrences of extremely

375   large buoyancy fluxes within the cloud. Connecting back to concepts discussed in the introduction, the coefficient correlation between the surface latent heat flux and the in-cloud buoyancy is 0.40, suggesting some evidence that a larger surface latent heat flux leads to a larger in-cloud buoyancy flux, as suggested by Bretherton and Wyant (1997) and Lewellen et al. (1996).

    Figure 11 displays the same information as that of Figure 10, except for TKE (Panel (a)) and TKE dissipation (Panel(c)). The total mean TKE was 0.132 ± 0.03 m^{2}s^{-2}, with a below-cloud mean of 0.133 ± 0.05 m^{2}s^{-2} and an in-cloud mean of

380   0.132 ± 0.04 m^{2}s^{-2}. The total mean ϵ was 3.97 ± 1.28 cm^{2}s^{-3}, with a below-cloud mean of 4.14 ± 2.45 cm^{2}s^{-3} and an in-cloud mean of 3.80 ± 1.81 cm^{2}s^{-3}. Overall, very consistent values (when looking at the means) between below-cloud and in-cloud exist, resulting in statistical similarity between the data populations for both TKE and ϵ. However, in looking at the boxplots, one can see that there are several cases (including Nov 1st and Nov 2nd) where the entire turbulent distribution of the below-cloud data is shifted to larger values than those of in-cloud data, with minimal overlap. This implies that the two layers

385   have limited mixing between them, perhaps due to a more turbulent decoupled lower boundary layer. This will be explored in further detail in Section 4.2. Along with having different turbulent distributions between in-cloud and below-cloud, both the TKE and the ϵ had maximum values on Nov 1st (0.163 m^2s^{-2} and 6.13 cm^2s^{-3}, respectively) and minimum values on Nov 2nd (0.065 m^2s^{-2} and 1.30 cm^2s^{-3}).

The analysis to this point clearly shows a maximum in turbulent properties on Nov 1st and a minimum on November 2nd.
390   This maximum is driven from turbulence below the cloud however, with the in-cloud TKE (0.128 m^2s^{-2}) and ϵ (2.78 cm^2s^{-3}) being below normal for in-cloud values, where the normal is 0.129 m^2s^{-2} and 3.68 cm^2s^{-3}, respectively. Panel (d) shows the total ϵ distribution for in-cloud and below-cloud. An increase in in-cloud frequency for ϵ is clear for the lowest values (first two histogram bars). Eight of the 15 measurements from the first two histogram bars came from RF11 and RF12 (Nov 1st and Nov 2nd), which includes all in-cloud values for those flights. The other seven measurements were all sampled above a normalized
395   boundary layer height of 0.90, suggesting entrainment mixing of stable laminar flow from the upper atmosphere into the upper boundary layer, reducing the turbulent energy.

It is important to analyze turbulent fluxes of energy, momentum, and moisture as they act to determine boundary layer structure and characteristics, along with analyzing how these variables are related to synoptic scale properties such as geopotential height. The correlation coefficients between boundary layer characteristics and synoptic scale properties can be found in Table
400   4. The 700-hPa geopotential height is fairly correlated with the boundary layer height, although this correlation is negative with a value of -0.37, suggesting that as the geopotential height increases, the boundary layer height decreases. The rate of change in the boundary layer height can be governed by:

$$\frac{dh}{dt} = \omega_e + \overline{\omega} \tag{9}$$

where h is boundary layer height, ω_e is the entrainment rate and ω is the synoptic scale vertical velocity (positive upwards).
405   This suggest that if the rate of subsidence increases to the point that it is larger than ω_e, then the boundary layer height will decrease with time. However, periods of ridging which lead to stronger synoptic scale subsidence aloft will also act to increase entrainment, resulting in a higher lifted condensation level (LCL) for entrained air, and a resulting increase in boundary layer height as a result. Given that h acts to decrease as the geopotential height increases, this suggests that the subsidence becomes the dominating component that governs h over that of entrainment. The correlation between entrainment zone thickness and the
410   boundary layer height is 0.22, in other words, as the geopotential height increases, both the boundary layer and the entrainment zone thickness decreases, and vice versa. Both TKE and ϵ increase in-cloud with respect to the geopotential height (correlation coefficient of 0.23 and 0.24, respectively) and decreases with respect to boundary layer height (-0.32 and -0.34, respectively).

As the cloud droplet number concentration and aerosol number concentration increase (accompanied by a decrease in average droplet size), the TKE and ϵ increase. Physically this makes sense, as precipitation is suppressed due to larger number
415   concentrations and smaller droplet sizes, a reduced moisture loss from the STBL can result, leading to thicker clouds, a larger buoyancy flux, and a larger TKE. Smaller droplets will also evaporate more readily, leading to enhanced latent heating effects and a resultant increase in turbulence. The correlation between the sensible heat flux and wind is the largest, with a value of

0.64, as expected since the sensible heat flux is expected to increase linearly with wind speed. The correlation between the boundary layer height and sensible heat flux is 0.36.

420   To summarize, the correlation coefficient values found here imply that the sensible heat flux is strongly correlated with wind speed, boundary layer height, and geopotential height, in agreement with Palm et al. (1999). It is found that as the boundary layer height decreases, TKE and ϵ tend to increase, along with the sensible and latent heat flux. The increased geopotential height (or decrease in boundary layer height), which is most strongly correlated with the sensible heat flux (0.56 and 0.49 for in-cloud and below-cloud, respectively), leads to enhanced values of sensible and latent heat and stronger turbulent values. The

425   various correlation coefficients indicate that (1) as the geopotential height decreases, the boundary layer height and entrainment zone increase, accompanied by a decrease of in-cloud and below-cloud turbulence; (2) as the geopotential height increases, the boundary layer height and entrainment zone decrease, accompanied by an increase of in-cloud and below-cloud turbulence. The observed decrease in boundary layer turbulence with increasing boundary layer height could be due to decoupling and an inability for the entire boundary layer to be mixed (leading to a subsequent decrease in turbulence), while a shallow boundary

430   layer can be easily mixed through cooling at cloud top.

4.2   Vertical Profiles

It has been shown through the boundary layer vertical structure in Figure 6 that the boundary layer is, on average, well mixed when considering thermodynamic variables. Figure 12 represents vertical profiles of the buoyancy flux (Panel (a)), latent heat flux (Panel (b)), vertical velocity variance (Panel(c)), and TKE (Panel (d)), where each dot represents a leg mean value, with

435   in-cloud values in red and values measured during Nov 1st and Nov 2nd in blue. The buoyancy flux in the subcloud layer (on average) varied between -2 and 20 Wm^{-2} and decreased with height until increasing within the cloud layer with values ranging between -5 and 43 Wm^{-2}. The standard deviation (in orange) was produced using data from vertical flight profiles as opposed to the horizontal legs due to data uniformity throughout the boundary layer depth. The buoyancy flux has a clear increase in variance within the cloud layer. The latent heat flux peaks near the surface, ranging between -1 and 55 Wm^{-2} below the cloud

440   layer and generally decreases with height. The variance peak of 33 Wm^{-2} occurs at a normalized boundary layer height of 0.99, displaying the variation in evaporative cooling due to entrainment mixing at cloud top between flight days.

    Vertical velocity variance (from here on $\overline{w'w'}$) ranged from 0.008 to 0.20 m^{2}s^{-2}. The observed in-cloud $\overline{w_iw_i}$ at Point Alpha was 0.105 m^{2}s^{-2} with values fluctuating considerably more than those in the subcloud layer. The average in-cloud value of $\overline{w'w'}$ found here is significantly lower than what was found over more remote ocean areas (80°W - 85°W, 20°S) of 0.36 m^{2}s^{-2}

445   (Bretherton et al., 2010). Nocturnal measurements of the Californian Sc deck during DYCOMS-II also revealed a stronger turbulent structure than that measured at Point Alpha, with observations showing in-cloud $\overline{w'w'}$ larger than 0.4 m^{2}s^{-2} with a maximum of 0.5 m^{2}s^{-2} near the base of the Sc deck (Stevens et al., 2005). As discussed in Wood (2012), $\overline{w'w'}$ is typically more vigorous at night due to the buoyancy production being larger from the lack of shortwave radiation absorption, which acts to stabilize the layer. As is found here, Hignett (1991) and Nicholls (1984) also found that $\overline{w'w'}$ peaked in the upper half

450   of the STBL away from any boundaries such as cloud top. Note that the TKE mirrors that of $\overline{w'w'}$ in terms of vertical spatial tendencies.

Considering data collected during aircraft soundings (as opposed to mean values of horizontal flight legs), u-variance, v-variance, w-variance, and the TKE are displayed in Figure 13 Panels (a) through (d), respectively, with the red line representing the mean profile and each gray line representing individual flight profiles. The blue lines represent flight profiles for Nov 1st

455 and Nov 2nd. Panel (e) displays the mean values from each of Panels (a) through (d). The profile of each variable in question shows a near constant value below cloud base, with an increase in-cloud before beginning to decrease near cloud top. Both $\overline{w'w'}$ and TKE reach their peak values at a normalized boundary layer height of 0.88 (or a normalized in-cloud location of 0.40). Simulations and observations from Pasquier and Jonas (1998) of in-cloud TKE showed that the maximum TKE occurred in two locations, near cloud top and near cloud base, suggesting that turbulence is being generated through two processes: (1) Cooling

460 at or near cloud top (through evaporation or longwave cooling), resulting in cool, dry downdrafts; (2) Warming near cloud base from the release of latent heat through condensation, resulting in positively buoyant updrafts. However, no conclusions can be made here on whether or not there are two sources of TKE due to the low vertical resolution of the mean values (i.e., averaging over 14 flight profiles). TKE values plummet above the inversion due to the dominance of clear, stable, and subsiding air aloft. The overall maximum in TKE measured (for all 14 flights) is found near a normalized boundary layer height of 0.60 (looking

465 at the blue profile line in Figure 13, Panel (d)) during RF11 (Nov 1st). This will be discussed in more detail in Section 4.3.

Looking at individual profiles of TKE, (not shown here), only six of the fourteen flights have a maximum TKE within the cloud layer. Modeling and observations of boundary layer profiles of turbulence from Pasquier and Jonas (1998) showed that mixing and overturning of the boundary layer profile due to buoyancy effects leads to a maximum in turbulence commonly being reached in the sub-cloud layer. Seven of the fourteen flights display two peaks in TKE within the cloud layer, one near

470 cloud base and another near cloud top, signifying evaporative cooling near cloud top and latent heating near cloud base. Of the six flights that have a maximum TKE within the cloud layer, all six display two peaks in the TKE within the cloud layer, one near cloud base and one near cloud top. Having the maximum in TKE in the subcloud layer can signify decoupling (Durand and Bourcy, 2001). A slight decoupling can lead to less moisture transport into the Sc layer, resulting in less latent heat release due to condensation. This could be why only one flight has two peaks in TKE within the cloud when the turbulence maximum

475 is reached below cloud, due to latent heat release at cloud base being suppressed.

Figure 14 displays the same information as Figure 13, except for values of buoyancy flux (Panel (a)), latent heat flux (Panel (b)), vertical velocity skewness (Panel (c)), and the cloud droplet number flux (Panel (d)). Note that Figure 14 displays the range of data in the gray envelope, as opposed to showing each individual profile with a single gray line. Both the buoyancy flux and the droplet number concentration flux (from here on w′N′) have maximum values at a normalized boundary layer

480 height of 0.93 (normalized in-cloud height of 0.59). The peak near cloud middle is due to a combination of the warm/moist updrafts and cool/dry downdrafts meeting, formed by evaporative cooling at cloud top and latent heating near cloud base. The same concept can be extended to w′N′, where droplets are activating near cloud base while evaporating near cloud top, suggesting that in the lower cloud the cloud droplet number concentration increases with updrafts (condensation), while the cloud droplet number concentration decreases with downdrafts (evaporation) in the upper cloud region. According to Pasquier

485 and Jonas (1998), the buoyancy flux should reach a minimum near cloud top from the entrainment of warm, dry air down into the cloud layer. Although the mean profile does not show a decrease at cloud top, the raw data (i.e., unsmoothed) does show a

negative buoyancy flux at cloud top. For individual flights, only RF11 (Nov 1st) had a maximum in the buoyancy flux in the subcloud layer. The latent heat flux peaks at the surface, but also sees a secondary maximum at a normalized boundary layer height of 0.99. The maximum at cloud top is due to entrainment of drier air from above the inversion down into the cloud (i.e.,

490   also a positive flux since both w' and q' are negative).

Well-mixed STBLs tend to show characteristics of downdrafts that are spatially smaller, but stronger, than updrafts. This results in a negative vertical velocity skewness (from here on $w'w'w'$) through most of the cloud and sub-cloud layer (Nicholls, 1989; Hogan et al., 2009). Panel (c) displays that $w'w'w'$ on average is negative throughout the cloud layer and through most of the subcloud layer, having a maximum value near the surface. The minimum values in $w'w'w'$ occurs at cloud base (normalized

495   in-cloud value of 0.04), suggesting that overall, the downdrafts are smallest, yet strongest at cloud base while updrafts are spatially larger, yet weaker.

Figure 15 shows the average buoyancy flux (Panel (a)), latent heat flux (Panel (b)), TKE (Panel (c)), and ϵ (Panel (d)) averaged over all flights for below-cloud and for different layers within the cloud. Each black dot represents the average value for individual flights using horizontal leg averages. The blue dots represent mean values using horizontal flight legs,

500   while the red dots represent mean values using flight vertical profile data. Values for in-cloud are calculated for layers between normalized in-cloud height values of 0-0.25 (cloud base), 0.25-0.50 (bottom middle), 0.50-0.75 (top middle), and 0.75-1 (cloud top). Table 5 summarizes the mean values for each layer. A clear difference in values and trends can be seen between sampling methods. For example, looking at the latent heat flux in Panel (b), we see that the horizontal leg sampling correctly captures the larger latent heat flux at the surface due to evaporation from the ocean surface, whereas the profile samples do not capture

505   this increase at the surface (the profile data is terminated at the start of the 30-m horizontal flight legs, meaning there is limited samples near the surface for the profile method). Conversely, the profile method observed a large increase in TKE at cloud top from evaporative cooling due to entrainment mixing, which is not observed in the horizontal leg method. Another example is the buoyancy flux, which is seen to have a large increase in-cloud as compared to below cloud using the profile method. The horizontal leg method displays a maximum in the top-middle region of the cloud, but the overall buoyancy flux increase in-

510   cloud vs. subcloud is compressed as compared to the profile method. In analyzing Table 5, it is clear that the average turbulence (both TKE and ϵ) peaks either in the bottom middle or top middle of the cloud (i.e., between a normalized cloud height of 0.25-0.75). This is also the two layers in which the buoyancy flux is at a maximum. TKE production near cloud base from latent heat release moves up through the cloud layer, while TKE production near cloud top from evaporative cooling moves down through the cloud layer, resulting in a maximum within the middle of the cloud.

515   Panels (e) and (f) represent the u, v, and w components of the TKE and ϵ, respectively. The anisotropic conditions present within the turbulent boundary flow can clearly be seen due to the differing values in each component. Although the u and v components are similar for most layers, differences are evident in the w-component. If the flow was perfectly isotropic, one would expect the same values for each component of the TKE and ϵ.

4.3 RF 11 (November 1st)

520 Turbulent and boundary layer characteristics have been shown to be abnormal on November 1st, with a minimum in 500-hPa Geopotential height, aerosol number concentration, and cloud droplet number concentration. November 1st also had overall mean maximum values of TKE and ϵ, in particular within the subcloud layer, along with maximum values in the surface sensible heat flux and drizzle rate. A moist layer is present above the boundary layer from looking at profiles of mixing ratio in Figure 6, leading to the secondary maximum in LWC and cloud thickness (November 2nd had the largest cloud thickness and

525 LWC). Also, visible in Figure 4 is the presence of wind shear near a normalized boundary layer height of 0.60.

Figure 16 shows profiles of multiple thermodynamic and turbulent variables as a function of normalized boundary layer height. Panel (a) shows profiles of potential temperature (blue), liquid water content (black), and mixing ratio (red). The gray envelope represents the cloud layer, while the orange envelopes represent areas in the subcloud layer where the sensible heat flux is negative and TKE and ϵ are enhanced. The potential temperature at the base of the lowest orange envelope begins to

530 deviate from its surface value, decreasing significantly. Normalizing the potential temperature from 0 to 1 (where the surface is 0 (the minimum temperature) and the top is 1 (the maximum temperature), we find that the value of the potential temperature is 0.32 at cloud top and 0.10 at cloud base, inferring significant entrainment of the warmer, less buoyant air aloft. However, the mixing ratio within the boundary layer stays relatively constant. This is due to the fact that the entrainment of the warmer air aloft has a larger mixing ratio that that near the surface of the boundary layer. Significant decoupling is occurring in the

535 subcloud layer, near a normalized boundary layer height of 0.60 (where the largest TKE and ϵ are located) and 0.40 (secondary maximum in the TKE and ϵ). It is suggested here that precipitation acts to decouple the boundary layer and enhance subcloud turbulence due to evaporative cooling of precipitation from the Sc deck above. Zheng et al. (2011) states that the cloud liquid water path reached a maximum on Nov, 1st and Nov 2nd due to the total-water specific humidity above the inversion being larger than that within the boundary layer. The inversion strength became significantly weaker on these two days (as evident

540 from Figure 7 and the boundary layer was decoupled due to drizzle.

As discussed previously, drizzle acts to warm the cloud layer and stabilizes the STBL, which reduces turbulent mixing and induces stratification. However, drizzle also evaporates readily below cloud base, resulting in evaporative cooling and enhanced instability for the subcloud layer (Wood, 2012). Precipitation promotes STBL decoupling by reducing the diabatic cooling in the cloud layer through in-cloud latent heating effects. The subcloud evaporation leads to cooling below cloud and a resultant

545 local minimum in the buoyancy flux is created (Bretherton and Wyant, 1997). The sensible heat flux (proxy for buoyancy) is observed to be negative from a normalized boundary layer height of ∼0.4 up to cloud base, with the minimum and local minimum outlined in the orange envelopes. The fact that turbulence peaks in the subcloud layer on this day is driven by the instability created from the cool layer below cloud base from precipitation. Normally, this will result in the cloud layer being decoupled form the surface moisture source, leading to a thinning cloud layer. However, the Sc deck is receiving moisture from

550 the upper atmosphere (as seen in the negative latent heat flux above cloud (where w' is negative but q^{prime} is positive). This process acts to moisten the boundary layer, which will lower the LCL, and assuming that the boundary layer height does not

change, this will thicken the cloud (Randall, 1984). Note that the cloud layer on Nov. 2nd is thicker than that on Nov. 1st by roughly 100 m.

Looking at $w'N'$, an increase occurs near cloud base up to the middle region of the cloud, before decreasing to negative
555 values in the upper half of the cloud. The positive values near cloud base occur due to droplet activation through condensation, while the negative values occur in the upper half of the cloud from upward vertical velocity perturbations having less droplets than that of negative vertical velocity perturbations, suggesting that droplet activation may be occurring near cloud top. The vertical velocity skewness also varies between positive and negative values within the subcloud layer, suggesting decoupling is occurring.

560 To summarize, it appears that the subcloud layer is decoupled from the Sc deck due to the evaporative cooling of precipitation. This increases turbulence within the subcloud layer, while reducing turbulence in the cloud layer. However, the cloud layer is still supplied with moisture through the entrainment of the more moist air aloft, driving cloud deepening and sustaining the Sc deck. The wind direction shifts from the south in the lower portion of the boundary layer to from the north near a normalized boundary layer height of 0.60. Seeing as the free atmosphere wind direction extends into the subcloud layer, this indicated that
565 significant entrainment mixing has occurred, resulting in the upper 40% of the boundary layer to share characteristics with the free atmosphere. Note that the maximum value in TKE that is measured on Nov. 1st at a boundary layer height of 0.60 (see the blue profile line in Figure 12), matching the location at which the wind shear is occurring. However, this spike in TKE cannot be attributed to the wind shear alone, as wind shear that occurs at the inversion for each flight day and within the boundary layer on Nov 4th do not result in large increases in turbulence. The increase in turbulence seen on Nov 1st is related to latent
570 heating affects and the resulting changes in the buoyancy fluxes. Although not displayed here, profiles for Nov 2nd (the day with the lowest average turbulence) shows a very consistent turbulent profile (no large spikes within or below the cloud layer), suggesting that precipitation has ceased and the boundary layer has been turned over, resulting in little energy remaining for mixing until cooling at cloud top becomes strong enough to support mixing again.

Comparing RF11 to a well-mixed boundary layer, Figure 17 displays the same information as that of Figure 16, except for
575 RF03 (Oct. 19th). Both potential temperature and mixing ratio appear to be well-mixed throughout the boundary layer, with a slight decrease in the potential temperature throughout the cloud layer. TKE, ϵ, the latent heat flux, and the sensible heat flux all have two peaks near cloud base and cloud top, suggesting latent heating near cloud base and evaporative cooling near cloud top. The sensible heat flux also has a negative value above cloud top due to the entrainment of warm, dry air down into the cloud from the stable air above the inversion. The droplet number concentration flux increases near cloud base owing to droplet
580 activation, and sees a sharp decrease near a normalized boundary layer of 0.50, suggesting most of the activation is occurring in the bottom half of the cloud layer. The vertical velocity skewness has a maximum negative value near cloud base, and never has an increase to positive values. The negative TKE flux within the cloud layer suggest that upward moving air is transporting less TKE than that of downward moving air. This negative TKE flux is proposed as evidence of the cloud top entrainment instability (CTEI) process, as proposed in Pasquier and Jonas (1998).

5 Conclusion

Variations in turbulent and meteorological properties within the boundary layer on a flight by flight basis (synoptic variation) have been examined. It has been shown that the influence of a synoptic system on Nov. 1st and Nov. 2nd leads to a deepening of the cloud layer during passage and a large increase in boundary layer height after passage. TKE is shown to be rather weak as compared to other observational studies of Sc decks. TKE is shown to vary around 0.13 m^2s^{-2}, except on the days leading up to and following the synoptic system passage, where the TKE increases rapidly to a maximum on Nov. 1st due to precipitation leading to enhanced turbulence in the subcloud layer and then decreases significantly to a minimum on Nov. 2nd. Vertical profiles of turbulent fluxes indicate:

– As the geopotential height decreases (increases), the boundary layer height and entrainment zone thickness increases (decreases), accompanied by a decrease (increase) of in-cloud and below-cloud turbulence.

– A maximum in TKE on Nov. 1st (both overall average and largest single value measured) is due to precipitation acting to destabilize the subcloud layer, while acting to stabilize the cloud layer. This is observed in both the vertical profiles of RF11 and the TKE and ϵ values in Figure 11, where it is shown that the distributions of turbulence for the subcloud and cloud layer are completely offset from one another, with the TKE in the subcloud layer maximizing for the analysis period, while the TKE in the cloud layer is below the average value for the analysis period.

– Six of the fourteen flights have a maximum TKE within the cloud layer. Seven of the fourteen flights display two peaks in TKE within the cloud layer, one near cloud base and another near cloud top, signifying evaporative cooling near cloud top and latent heating near cloud base. Of the six flights that have a maximum TKE within the cloud layer, all six display two peaks in the TKE within the cloud layer, one near cloud base and one near cloud top.

– Analyzing different layers of turbulence over the 14 flights shows that TKE, ϵ, and the buoyancy flux, on average, all reach maximum values near cloud middle (between normalized in-cloud values of 0.25- 0.75).

The results presented here represent a snapshot of data through 14 aircraft flights, with at least a day between any two flights. Therefore, the results presented represent boundary layer conditions that were present at the time of measurement, limiting any analysis of continuously evolving boundary layer and turbulent conditions, for example, being able to analyze the changing thermodynamic and dynamic conditions that resulted in large turbulent changes between Nov 1st and Nov 2nd. It has also been displayed that how turbulence is analyzed is important to understanding the true extent of how turbulence varies within the boundary layer. Taking large scale averages of turbulent parameters (such as over entire horizontal flight legs) may lead to important smaller resolution variations being averaged out. For example, the vertical profiles presented in Figures 16 and 17 show much more detail in the vertical trends as compared to the averaged results of horizontal leg means displayed in Figure 12. Future work will involve using the turbulent analysis presented here to better understand the interactions between droplet clustering (or preferential concentration) and turbulence within Sc clouds, including variables that may influence the components just mentioned, such as aerosol number concentration, cloud height, and precipitating vs. non-precipitating regions of cloud.

Data availability. All cabin data from different aircraft platforms can be found on the VOCALS-Rex website at https://archive.eol.ucar.edu/
projects/vocals/rex.html (last access: 02 February 2020). All NCEP/NCAR reanalysis data can be found from NOAA at https://www.esrl.noaa
620 .gov/psd/data/gridded/data.ncep.reanalysis.html.

Author contributions. DSD and JDSG contributed equally to both the analysis and the writing of this paper.

Competing interests. There are no competing interests to declare

Acknowledgements. We thank the CIRPAS Twin Otter crew and personnel, including pilots Mike Hubble and Chris McGuire, for their effort
and support during the field program, along with any individual who contributed to the planning and execution of VOCALS-Rex. This work
625 was funded by NASA NESSF grant 80NSSC18K1406.

References

Albrecht, B., Randall, D. A., and Nicholls, S.: Observations of marine stratocumulus during FIRE, Bull. Amer. Meteor. Soc., 69, 619–626, 1988.

Albrecht, B. A., Jensen, M. P., and Syrett, W. J.: Marine boundary layer structure and fractional cloudiness, J. Geophys. Res., 100, 14 209–14 222, 1995.

Barret, B. S., Garreaud, R. D., and Falvey, M.: Effect of the Andes cordillera on precipitation from a midlatitude cold front, Mon. Weather Rev., 137, 3092–3109, 2009.

Bretherton, C. S. and Wyant, M. C.: Moisture transport, lower-tropospheric stability, and decoupling of cloud-topped boundary layers, J. Atmos. Sci., 54, 148–167, 1997.

Bretherton, C. S., Uttal, T., Fairall, C. W., Yuter, S. E., Weller, R. A., Baumgardner, D., Comstock, K., Wood, R., and Raga, G. B.: The Epic 2001 Stratocumulus Study, B. Am. Meteorol. Soc., 85, 967–977, 2004.

Bretherton, C. S., Uchida, J., and Blossey, P.: Slow manifolds and multiple equilibria in stratocumulus-capped boundary layers, J. Adv. Model. Earth Syst., 2, https://doi.org/10.3894/JAMES.2010.2.14., 2010.

Caughey, S. J., Crease, B. A., and Roach, W. T.: A field-study of nocturnal stratocumulus. 2. Turbulence structure and entrainment, Quart. J. Roy. Meteor. Soc., 108, 125–144, 1982.

Chamecki, M. and Dias, N. L.: The local isotropy hypothesis and the turbulent kinetic energy dissipation rate in the atmospheric surface layer, Q. J. Roy. Meteor. Soc., 130, 2377–2752, 2004.

Chapman, D. and Browning, K. A.: Measurements of dissipation rate in frontal zones, Quart. J. Roy. Meteor. Soc., 127, 1939–1959, 2001.

de Roode, S. R. and Duynkerke, P. G.: Dynamics of cumulus rising into stratocumulus as observed during the first 'Lagrangian' experiment of ASTEX, Quart. J. Roy. Meteor. Soc., 122, 1597–1623, 1996.

Durand, P. and Bourcy, T.: Observations of the turbulence structure wihtin two stratocumulus-topped, marine boundary layers, Boundary Layer Meteorology, 99, 105–125, 2001.

Frank, H. P.: Boundary layer structure in two fronts passing a tower, Meteor. Atmos. Phys., 53, 95–109, 1994.

Frisch, U.: Turbulence–The Legacy of A. N. Kolmogorov, Cambridge University Press, 1995.

Garreaud, R. D. and Rutllant, J.: Coastal Lows along the Subtropical West Coast of South America: Numerical Simulation of a Typical Case, Mon.Weather Rev., 131, 891–908, 2003.

Hignett, P.: Observations of diurnal variation in a cloud-capped marine boundary layer, J. Atmos. Sci., 48, 1471–1482, 1991.

Hogan, R. J., Grant, L., Illingworth, A. J., Pearson, G. N., and O'connor, E. J.: Vertical velocity variance and skewness in clear and cloud-topped boundary layers as revealed by Doppler Lidar, Quart. J. Roy. Meteor. Soc., 135, 635–643, 2009.

Jen-La Plante, I., Ma, Y., Nurowska, K., Gerber, H., Khelif, D., Karpinska, K., Kopec, M. K., Kumala, W., and Malinowski, S. P.: Physics of Stratocumulus Top (POST): turbulence characteristics, Atmos. Chem. Phys., 16, 9711–9725, 2016.

Kistler, R., Kalnay, E., Collins, W., Saha, S., White, G., Woollen, J., Chelliah, M., Ebisuzaki, W., Kanamitsu, M., Kousky, V., can den Dool, H., Jeene, R., and Fiorino, M.: The NCEP-NCAR 50-Year Reanalysis: Monthly Means CD-ROM and Documentation, B. Am. Meteorol. Soc., 82, 247–267, 2001.

Kolmogorov, A. N.: The local structure of turbulence in incompressible viscous fluid for very large Reynolds numbers, Dokl. Akad. Nauk SSSR, 30, 301–304, 1941.

Lewellen, D. C., Lewellen, W. S., and Yoh, S.: Influence of Bowen ratio on boundary layer cloud structure, J. Atmos. Sci., 53, 175–187, 1996.

Lilly, D. K.: Models of cloud-topped mixed layers under a strong inversion, Quart. J. Roy. Meteor. Soc., 94, 292–309, 1968.

665 Moeng, C. H., Shen, S. H., and Randall, D. A.: Physical processes within the nocturnal stratus-topped boundary layer, J. Atmos. Sci., 49, 2384–2401, 1992.

Nicholls, S.: The dynamics of stratocumulus: Aircraft obser- vations and comparisons with a mixed layer model, Quart. J. Roy. Meteor. Soc., 110, 783–820, 1984.

Nicholls, S.: The structure of radiatively driven convection in stratocumulus, Quart. J. Roy. Meteor. Soc., 115, 487–511, 1989.

670 Nicholls, S. and Leighton, J.: An observational study of the structure of stratiform cloud sheets: Part I. Structure, Quart. J. Roy. Meteor. Soc., 112, 431–460, 1986.

Palm, S. P., Schwemmer, G. K., Vandemark, D., Evans, K. D., and Miller, D. O.: The estimation of surface latent heat flux over the ocean and its relationship to Marine Atmospheric Boundary Layer (MABL) structure, Proc. SPIE, https://doi.org/10.1117/12.366432, 1999.

Pasquier, J. R. M. and Jonas, P. R.: Turbulent transport in fields of warm cumulus clouds, Quart. J. Met. Soc., 124, 363–387, 1998.

675 Pinsky, M. B. and Khain, A. P.: Simulations of drop fall in a homogeneous isotropic turbulent flow, Atmos. Res., 40, 223–259, 1996.

Rahn, D. A. and Garreaud, R.: Marine boundary layer over the subtropical southeast Pacific during VOCALS-REx – Part 2: Synoptic variability, Atmos. Chem. Phys., 10, 4507–4519, 2010.

Randall, D. A.: Stratocumulus cloud deepening through entrainment, Tellus, 36A, 446–457, 1984.

Randall, D. A., Coakley, J. A., Fairall, C. W., Knopfli, R. A., and Lenschow, D. H.: Outlook for research on marine subtropical stratocumulus

680 clouds, Bull. Amer. Meteor. Soc., 64, 1290–1301, 1984.

Schubert, W. H., Wakefield, J. S., Steiner, E. J., and Cox, S. K.: Marine stratocumulus convection. Part I: Governing equations and horizontally homogeneous solutions, J. Atmos. Sci., 36, 1286–1307, 1979.

Shapiro, M. A., Hampel, T., Rotzoll, D., and Mosher, F.: The frontal hydraulic head: A microscale (1 km) triggering mechanism for mesoconvective weather systems, Mon. Wea. Rev., 113, 1166–1183, 1985.

685 Shaw, R. A.: Particle–Turbulence Interactions in Atmospheric Clouds, Annu. Rev. Fluid Mech., 35, 183–227, 2003.

Siebert, H., Lehmann, K., and Wendisch, M.: Observations of small-scale turbulence and energy dissipation rates in the cloudy boundary layer, J. Atmos. Sci., 63, 1451–1466, 2006.

Stevens, B., Moeng, C.-H., Ackerman, A. S., Bretherton, C. S., Chlond, A., de Roode, S., Edwards, J., Golaz, J.-C., Jiang, H., Khairoutdinov, M., Kirkpatrick, M. P., Lewellen, D. C., Lock, A., Muller, F., Stevens, D. E., Whelan, E., and Zhu, P.: Evaluation of large-eddy simulations

690 via observations of nocturnal marine stratocumulus, Mon. Wea. Rev., 133, 1443–1462, 2005.

Taylor, P. A., Salmon, J. R., and Stewart, R. E.: Mesoscale observations of surface fronts and low pressure centres in Canadian East Coast storms, Bound. Layer Meteor., 64, 15–54, 1993.

Toniazzo, T., Abel, S. J., Wood, R., Mechoso, C. R., Allen, G., and Shaffrey, L. C.: Large-scale and synoptic meteorology in the south-east Pacific during the observations campaign VOCALS-REx in austral Spring 2008, Atmos. Chem. Phys., 11, 4977–5009, 2011.

695 Wood, R.: Stratocumulus Review, Mon. Weather Rev., 140, 2373–2423, 2012.

Wood, R. and Bretherton, C. S.: Boundary Layer Depth, Entrainment, and Decoupling in the Cloud-Capped Subtropical and Tropical Marine Boundary Layer, J. Climate, 17, 3576–3588, 2004.

Wood, R. and Hartmann, D. L.: Spatial variability of liquid water path in marine boundary layer clouds: The importance of me- soscale cellular convection, J. Climate, 19, 1748–1764, 2006.

700 Wood, R., Mechoso, C. R., Bretherton, C. S., Weller, R. A., Huebert, B., Straneo, F., Albrecht, B. A., Coe, H., Allen, G., Vaughan, G., Duam, P., Fairall, C., CHand, D., Klenner, L. G., Garreaud, R., Grados, C., Covert, D. S., Bates, T. S., Krejci, R., Russell, L. M., de Szoeke, S., Brewer, A., Yuter, S. E., Springston, S. R., Chaigneau, A., Toniazzo, T., Minnis, P., Palikonda, R., Abel, S. J., Brown, W. O. J., Williams, S., Fochesatto, J., Brioude, J., and Bower, K. N.: The VAMOS Ocean-CLoud-Atmosphere-Land Study Regional Experiment (VOCALS-Rex): goals, platforms, and field operations, Atmos. Chem. Phys., 11, 627–654, 2011.

705 Wyant, M. C., Wood, R., Bretherton, C. S., Mechoso, C. R., Bacmeister, J., Balmaseda, M. A., Barrett, B., Codron, F., Earnshaw, P., Fast, J., Hannay, C., Kaiser, J. W., Kitagawa, H., Klein, S. A., Kohler, M., Manganello, J., Pan, H. L., Sun, F., Wang, S., and Wang, Y.: The PreVOCA experiment: modeling the lower troposphere in the Southeast Pacific, Atmos. Chem. Phys., 10, 4757–4774, 2010.

Young, G. S. and Johnson, R. H.: Meso and microscale features of a Colorado cold front, J. Climate Appl. Meteor., 23, 1315–1325, 1984.

Zheng, X., Albrecht, B. A., Minnis, P., Ayers, K., and Jonson, H. H.: Observed aerosol and liquid water path relationships in marine stra-
710   tocumulus, Geophys. Res. Lett., 37, L17 803, 2010.

Zheng, X., Albrecht, B., Jonsson, H. H., Khelif, D., Feingold, G., Minnis, P., Ayers, K., Chuang, P., Donaher, S., Rossiter, D., Ghate, V., Ruiz-
Plancarte, J., and Sun-Mack, S.: Observations of the boundary layer, cloud, and aerosol variability in the southeast Pacific near-coastal marine stratocumulus during VOCALS-REx, Atmos. Chem. Phys., 11, 9943–9952, 2011.
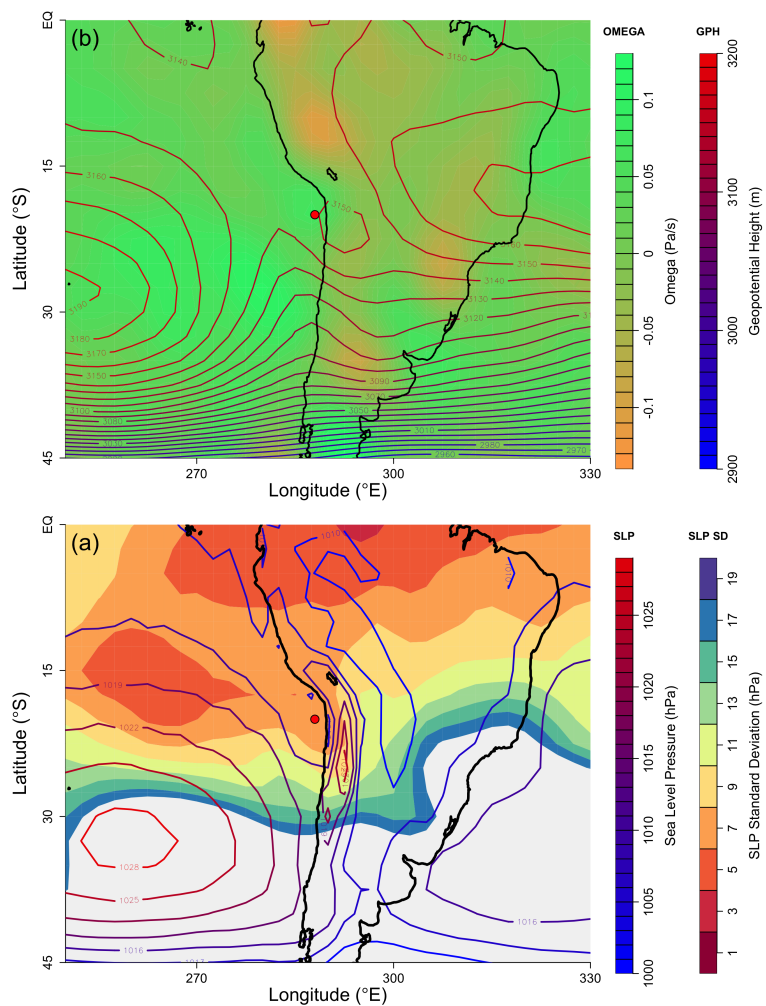
Figure 1. Panel (a): Mean sea level pressure (hPa) between October 19th and November 12th with the standard deviation overlaid. Note that the contours are every 3-hPa; Panel(b): Mean 700-hPa geopotential height with mean omega overlaid at the same level. Contours are every 10-m. The red dot in both panels represents the location of Point Alpha.
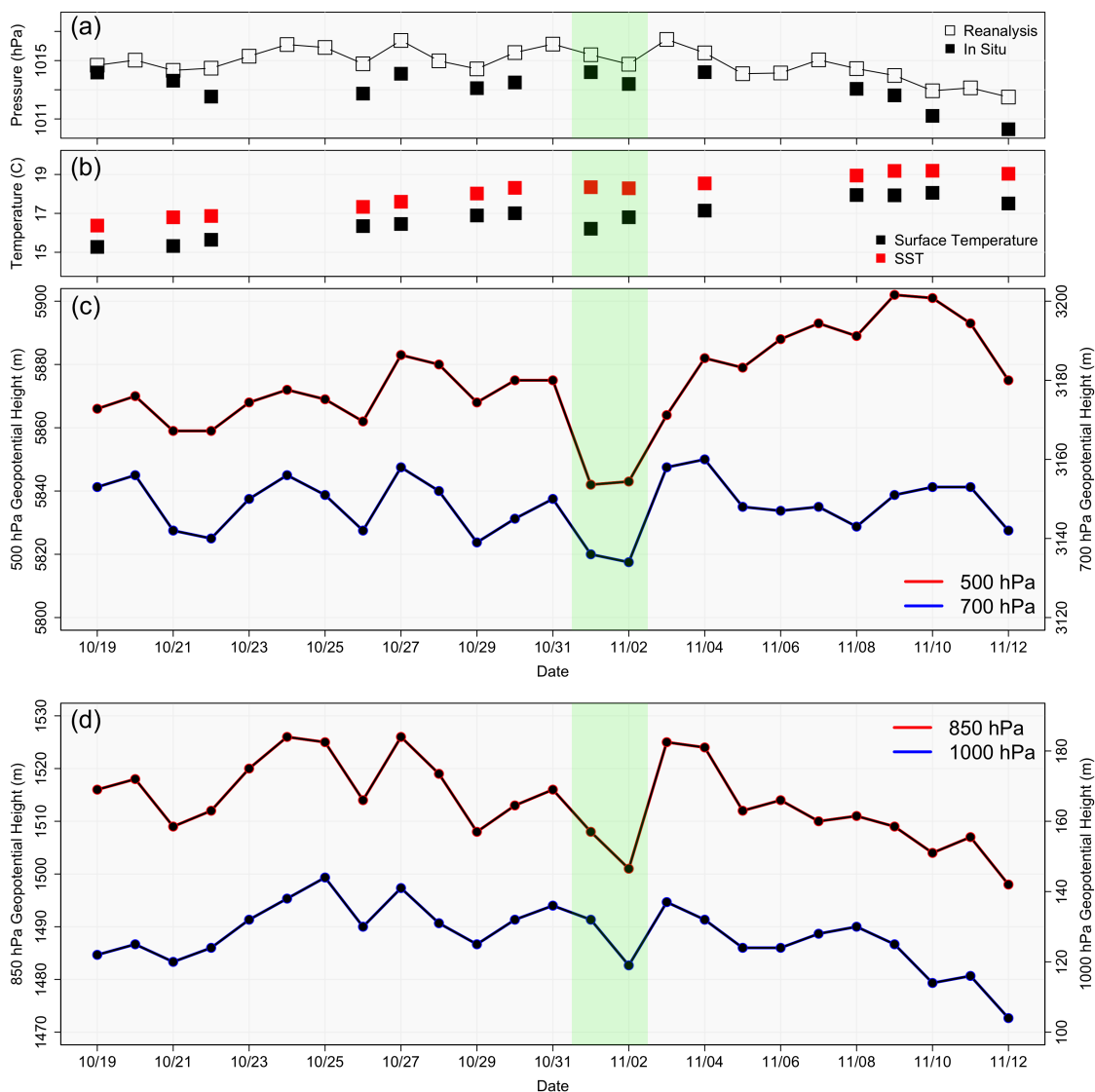
Figure 2. Panel (a): NCEP/NCAR reanalysis (open squares) and flight data (solid squares); Panel (b): Sea surface temperature and at-
mospheric surface temperature collected from flight data; Panel (c): 500-hPa (red) and 700-hPa (blue) geopotential height data from
NCEP/NCAR reanalysis data; Panel (d): Same as panel (c), except for 850-hPa (red) and 1000-hPa (blue).
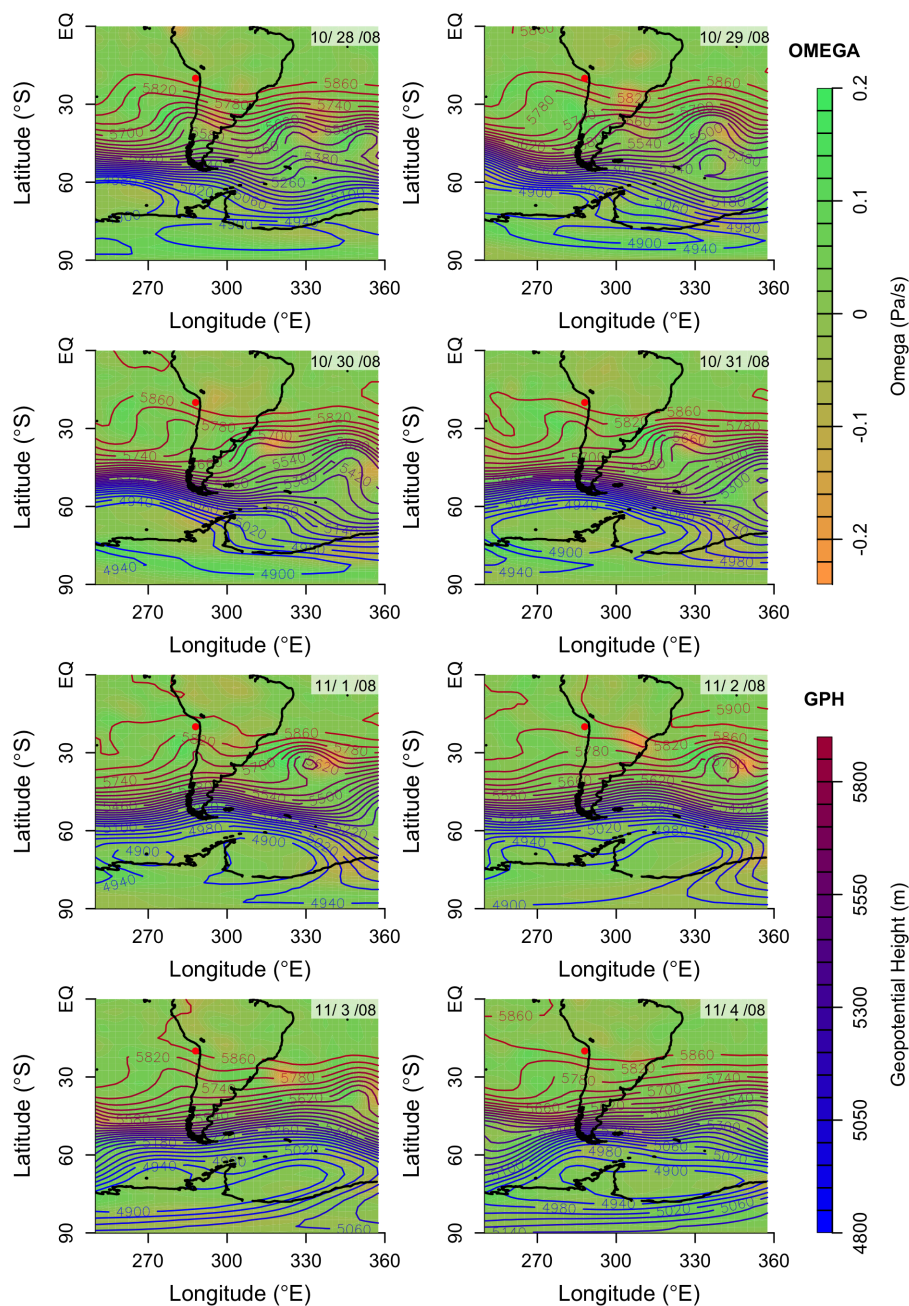
Figure 3. Spatial maps spanning 10/28/08 (top-left) to 11/4/08 (bottom-right) of 700-hPa geopotential height (solid line contours) with 700-hPa omega values overlaid using filled contours.
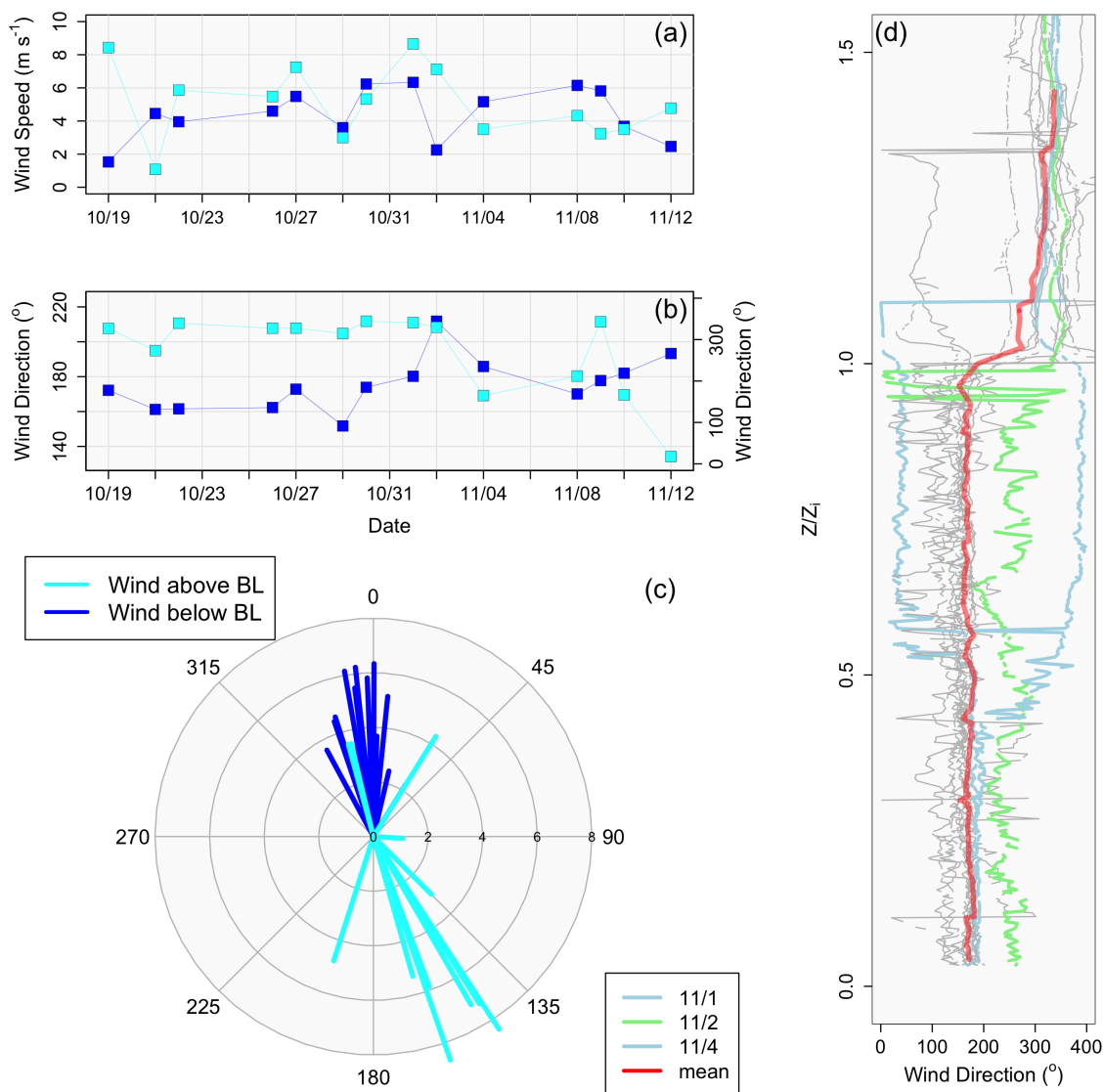
Figure 4. Panel(a): Wind speed (ms^{-1}) at the surface collected during 30-m horizontal flight legs (dark blue) and above the inversion collected during horizontal flight legs above the boundary layer (light blue); Panel (b): Same as panel (a), except for wind direction (degree); Panel (c): Vectors showing wind direction from panel (b); Panel (d): Vertical profiles (collected during aircraft soundings) of wind direction for each flight day plotted vs. normalized boundary layer height. November 1st and 4th are displayed in light blue, November 2nd is green, and the mean wind direction is represented by red.
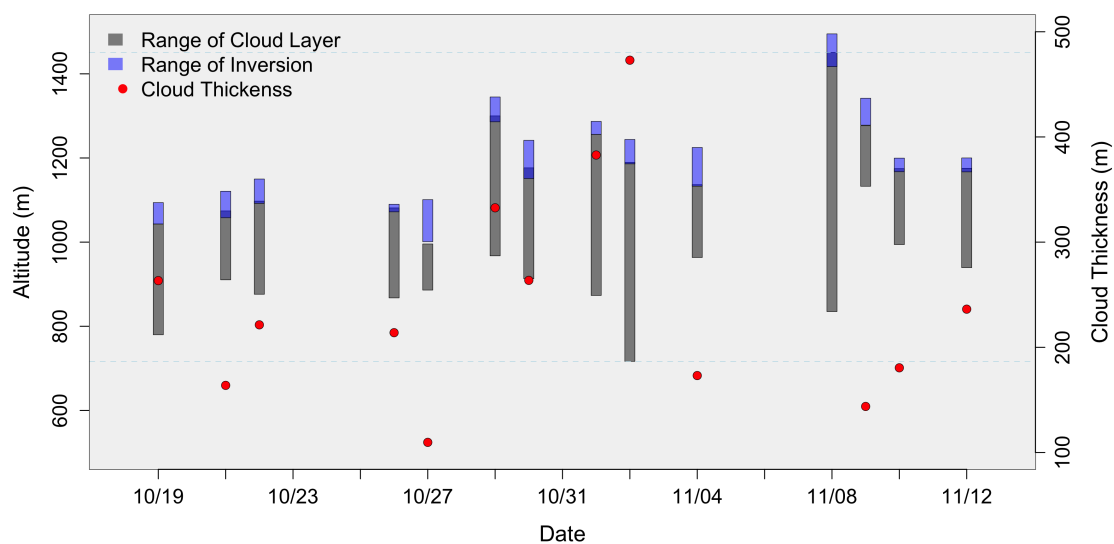
Figure 5. Shows the range of the cloud (gray) and inversion (blue) layer as a function of altitude for each RF. The top of each gray profile represents cloud top and boundary layer top. The bottom of each gray profile represents cloud base. Cloud thickness (represented as a single value) is represented by each red dot (right y-axis).
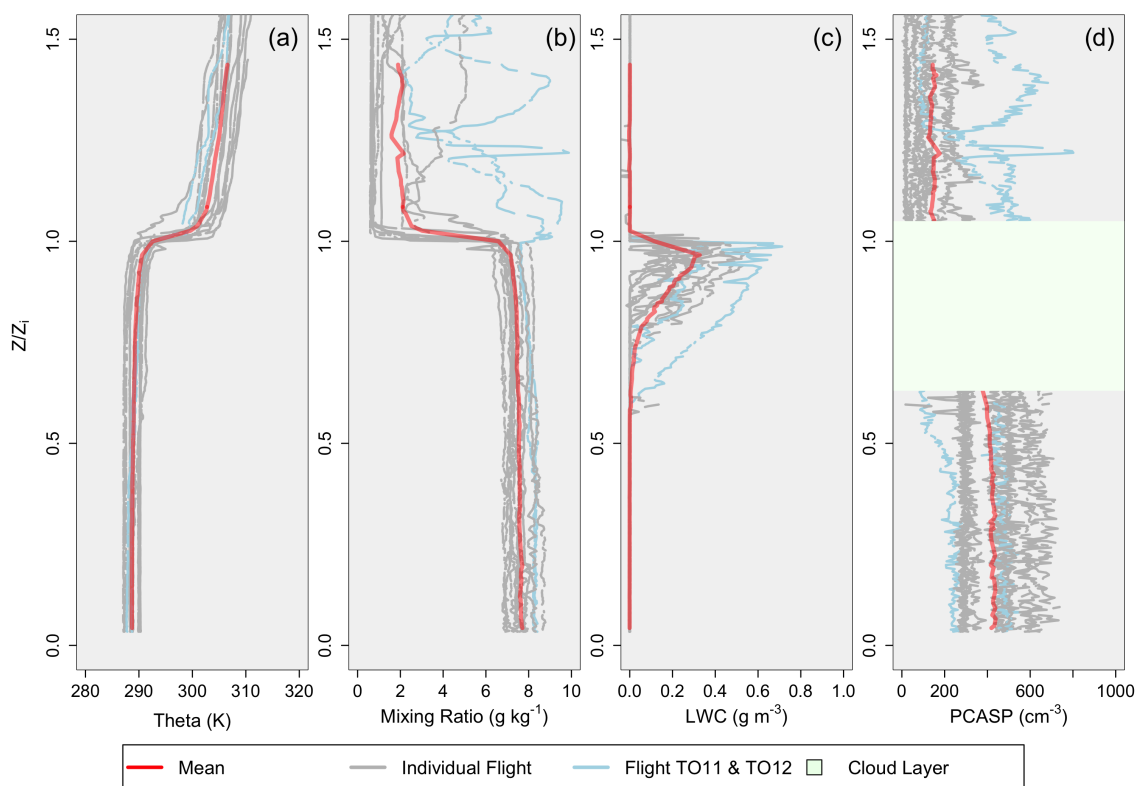
Figure 6. Profiles scaled by the boundary layer heights. (a) potential temperature (K); (b) mixing ratio (g kg^{-1}); (c) liquid water content (g m^{-3}); (d) Aerosol number concentration (cm^{-3}). The red profile represents the mean value, and the two blue profiles represent RF 11 and RF 12. The green layer represents the relative cloud layer for panel (d), as aerosol data cannot be collected in the cloud layer.
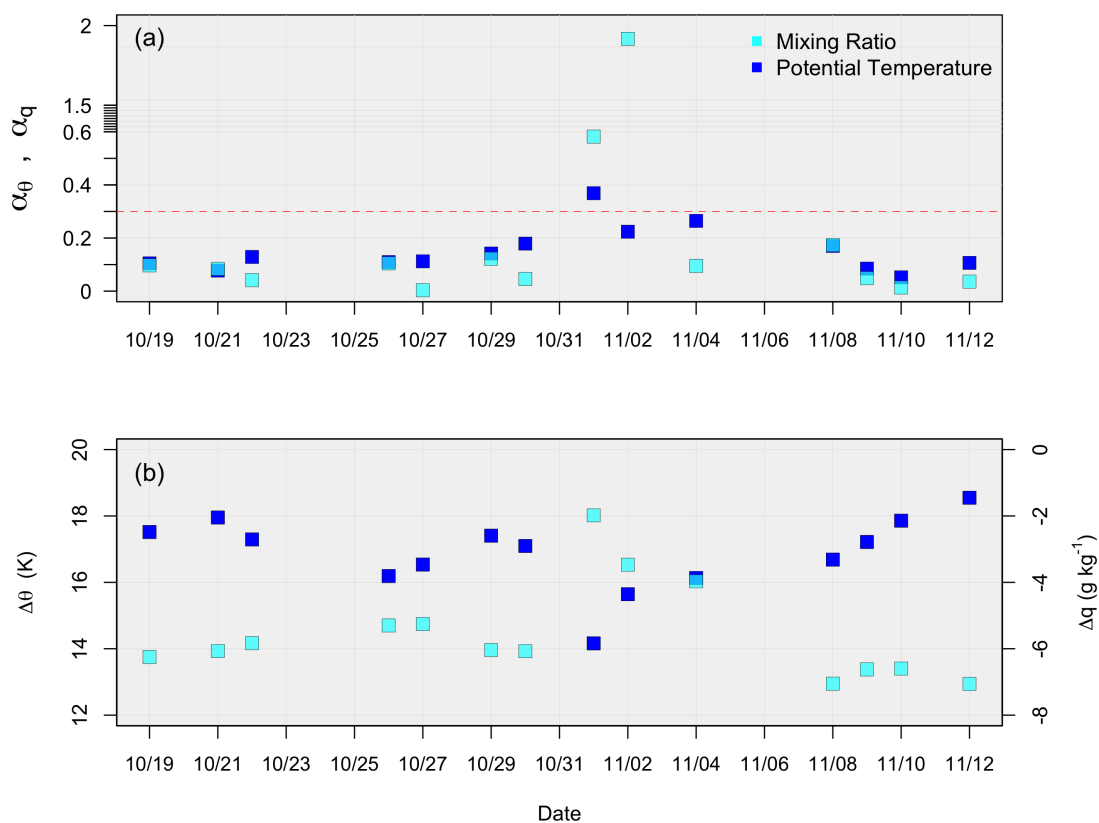
Figure 7. (a) The decoupling parameters; (b) potential temperature (left y-axis) and mixing ratio (right y-axis) differences across the inversion, for all 14 flights.
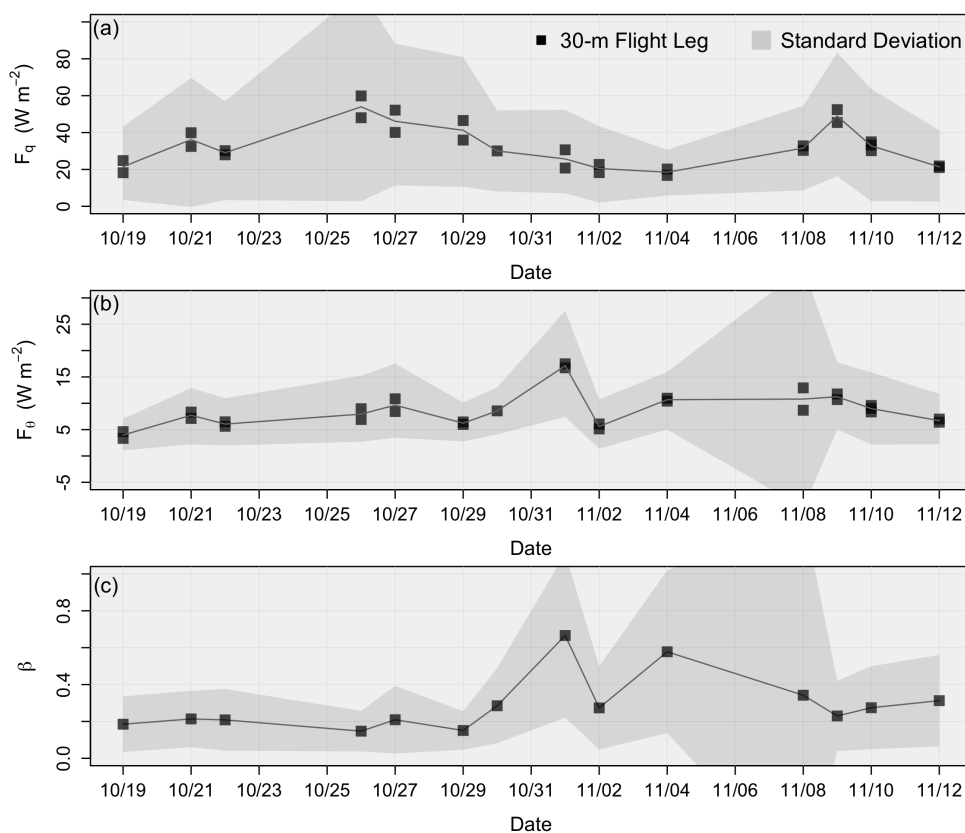
Figure 8. Values of (a) surface latent heat flux (Wm^{-2}); (b) Sensible heat flux (Wm^{-2}); and (c) the Bowen ratio, for each flight day. Note that each black square is a mean of a 30-m horizontal flight leg, while the gray envelope represents the standard deviation.
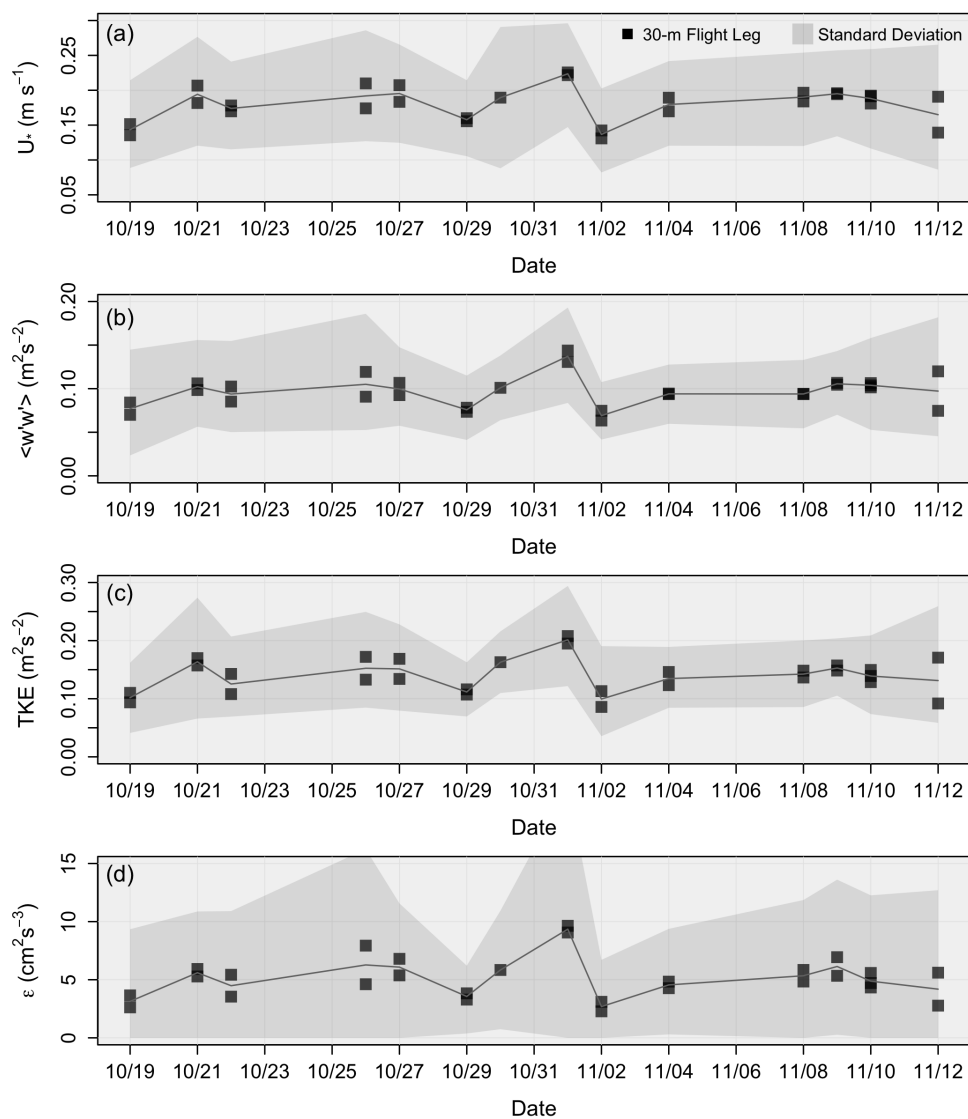
Figure 9. As in Figure 8, except for (a) Friction velocity (m^2s^{-2}); (b) Vertical velocity variance (m^2s^{-2}); (c) Turbulent kinetic energy (m^2s^{-2}); (d) Turbulent kinetic energy dissipation rate (cm^2s^{-3}).
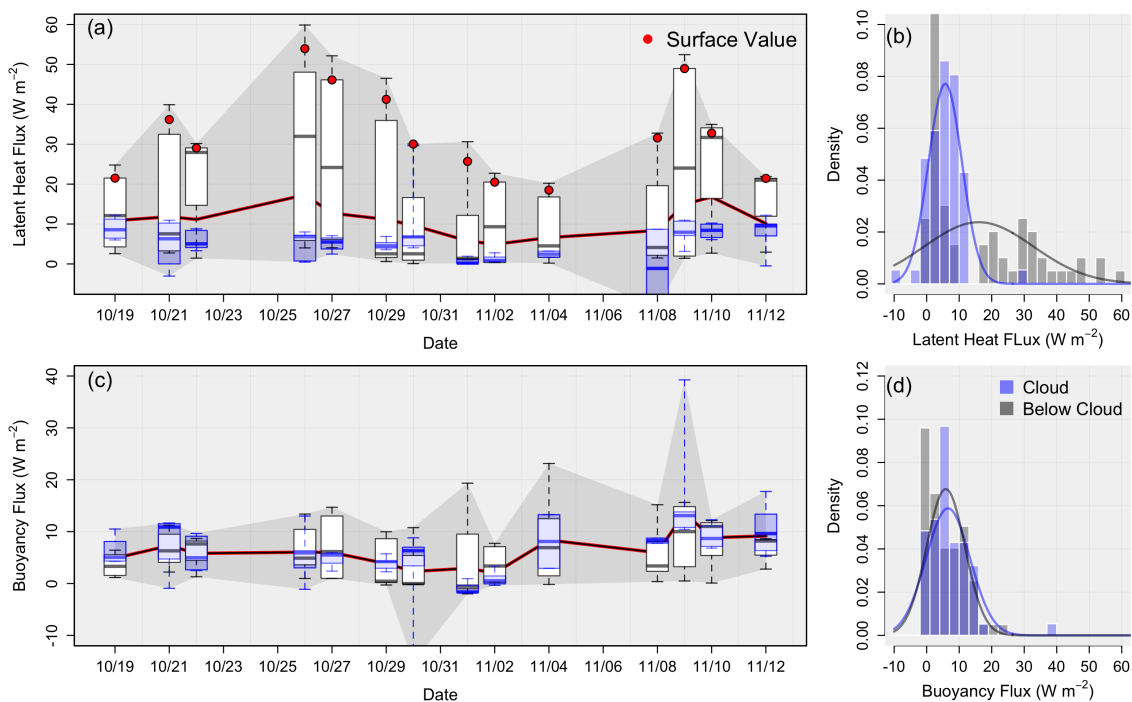
Figure 10. Boxplots of in-cloud (blue) and below cloud (white) data using mean values of horizontal flight legs for (a) the latent heat flux (Wm^{-2}) and (c) the Buoyancy flux (Wm^{-2}). Note that the gray envelope represents the range of the data, while the red line represents each flight mean values. Panels (b) and (d) shows the distributions of the data populations (with normal distributions overlaid for reference) for the latent heat flux and buoyancy flux, respectively.
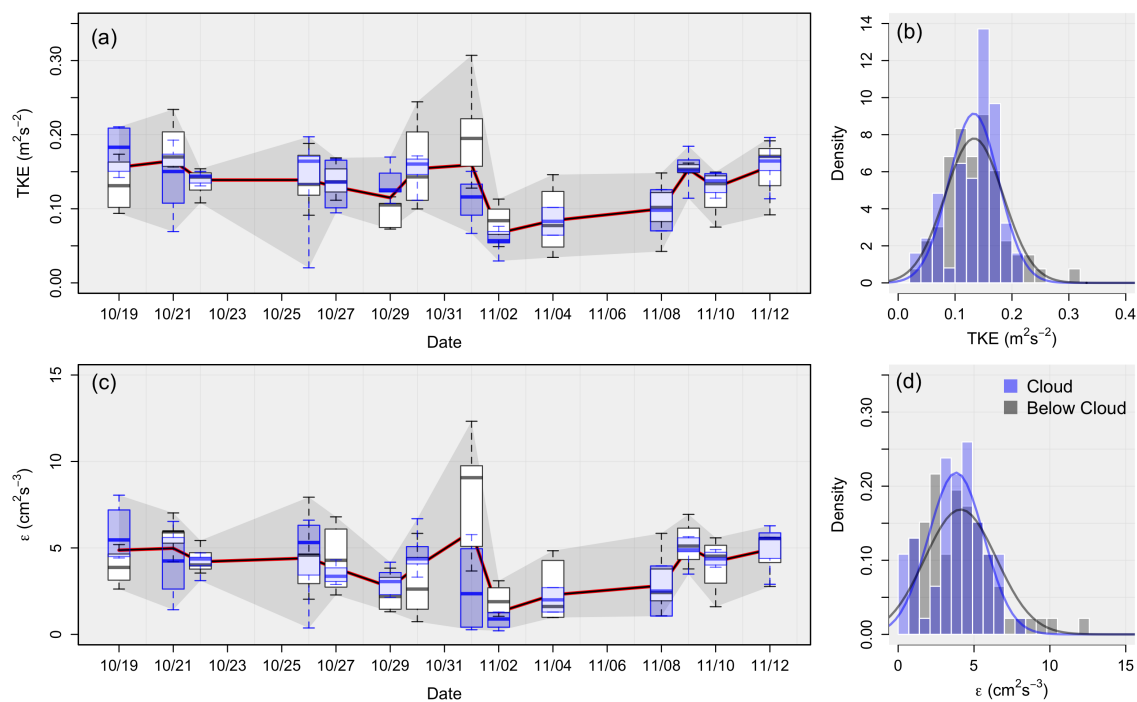
Figure 11. As in Figure 10, except for TKE (m^2s^{-2}) in (a) and (b) and ϵ ($cm^{-2}s^{-3}$) in (c) and (d)
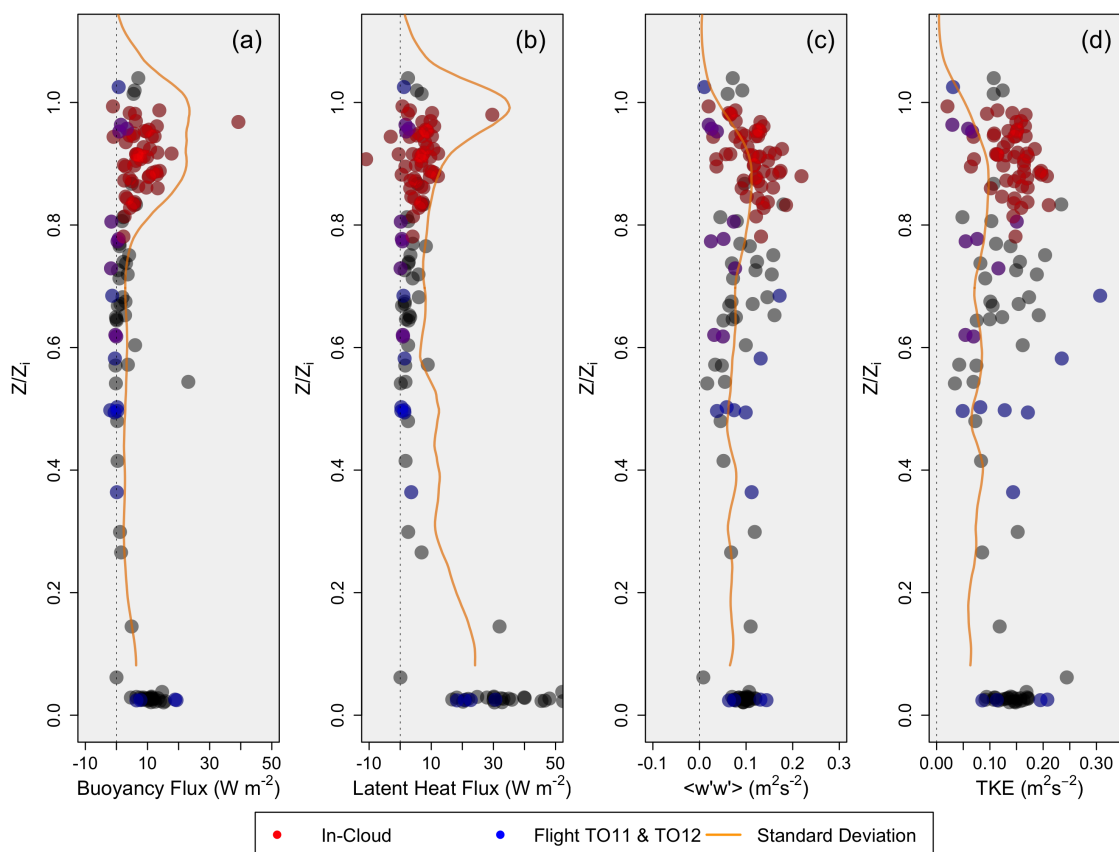
Figure 12. Mean values of horizontal flight legs plotted as a function of normalized boundary layer height. In-cloud data is red while data collected during Nov. 1st and 2nd is blue. The standard deviation is represented in orange. (a) Buoyancy flux (Wm^{-2}); (b) Latent heat flux (Wm^{-2}); (c) Vertical velocity variance (m^{2}s^{-2}); (d) TKE (m^{2}s^{-2}).
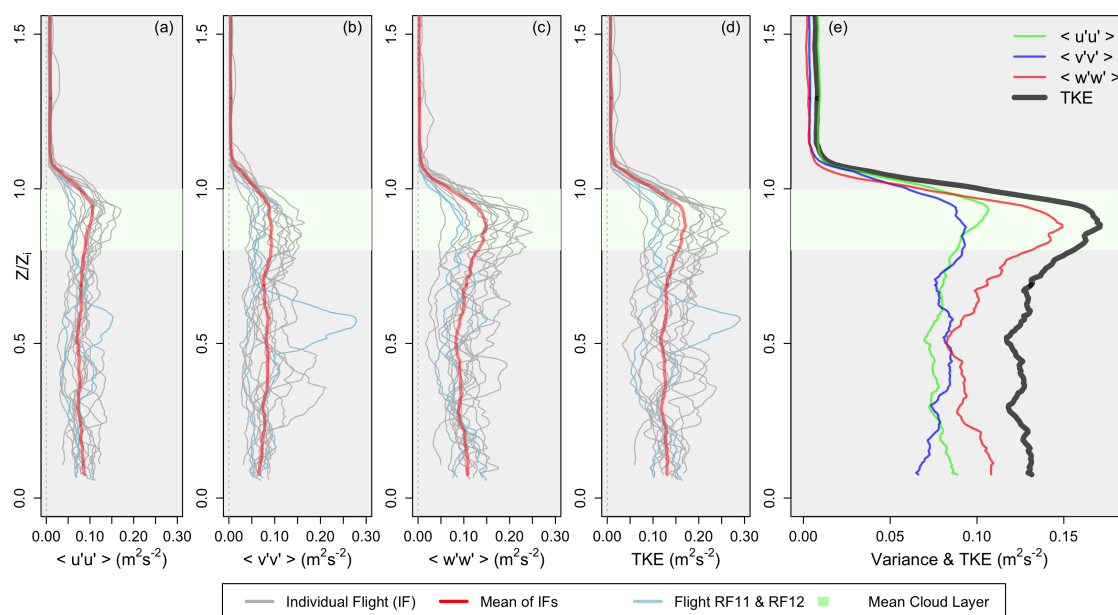
Figure 13. Vertical profiles (from data collected during flight profiles) of (a) u-variance (m^2s^{-2}); (b) v- variance (m^2s^{-2}); (c) w-variance (m^2s^{-2}); (d) TKE (m^2s^{-2}). Individual flights are displayed in gray, the mean value is displayed in red, with RF11 and RF12 shown in blue. Panel (e) shows the mean values from each of panels (a) through (d)
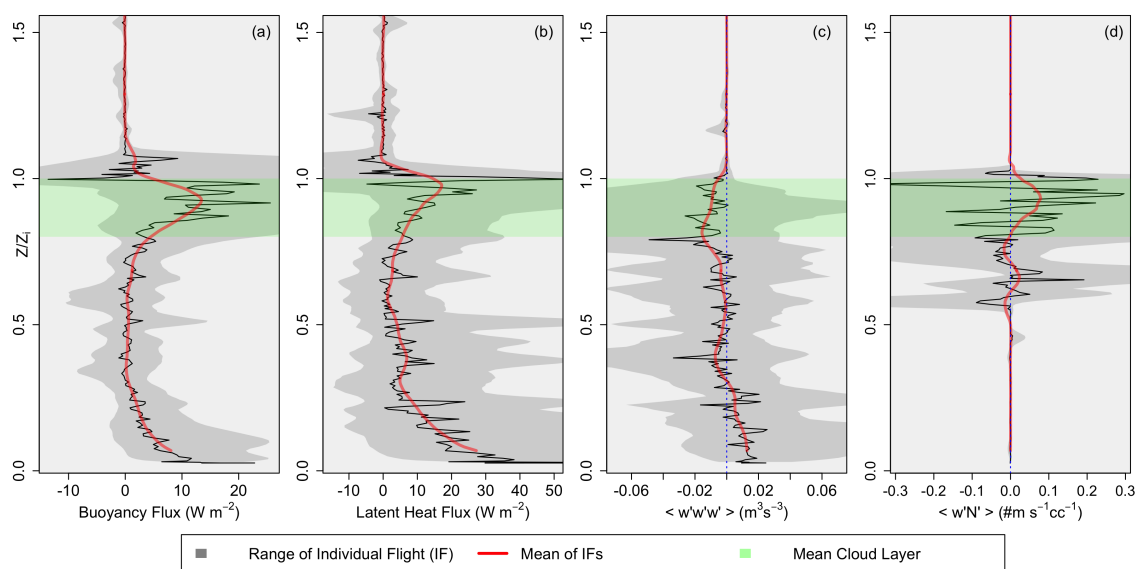
Figure 14. Vertical profiles (from data collected during flight profiles) of (a) Buoyancy flux (Wm^{-2}); (b) Latent heat flux (Wm^{-2}); (c) Vertical velocity skewness (m^{3}s^{-3}); (d) cloud droplet flux (ms^{-1}cc^{-1}). Note that the red line is the smoothed average of the raw data (black), while the gray envelope represents the range of values encountered.
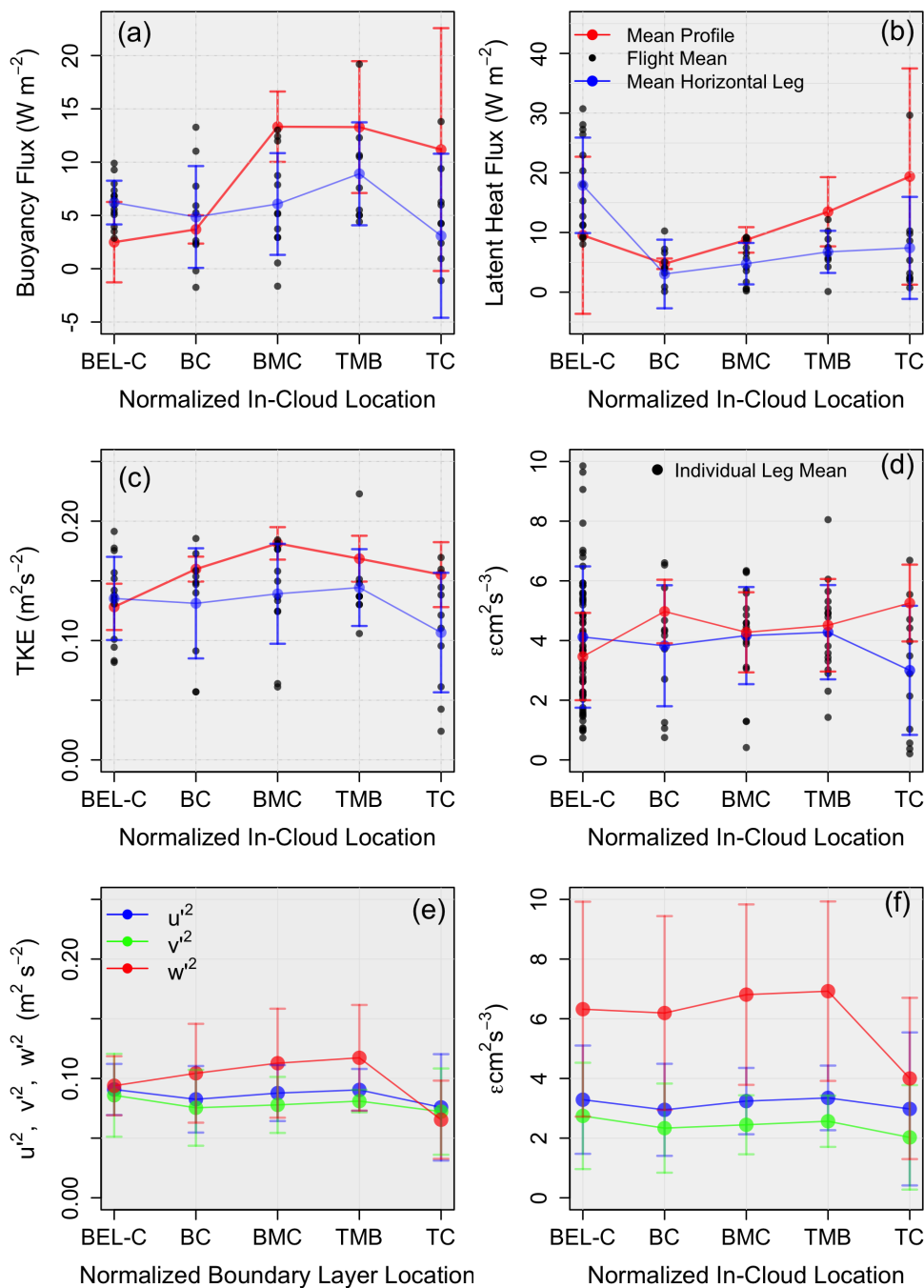
Figure 15. (a) Buoyancy flux (Wm^{-2}); (b) Latent heat flux (Wm^{-2}); (c) TKE (m^{2}s^{-2}); (d) TKE dissipation rate (cm^{2}s^{-3}). Data is divided into layers, including below-cloud (BEL-C), bottom of cloud (BC), bottom-middle of cloud (BMC), top-middle cloud (TMC), and top of cloud (TC). Red represents mean values for each layer using data collected during flight vertical profiles while blue represents mean values for each layer using data collected during horizontal flight legs. Black dots represent mean values for each flight using horizontal flight leg data. Note that the black dots in Panel (e) represent individual leg mean values as opposed to mean flight values. Panels (e) and (f) represent u (blue), v (green), and w (red) components of the TKE and TKE dissipation rate, respectively.
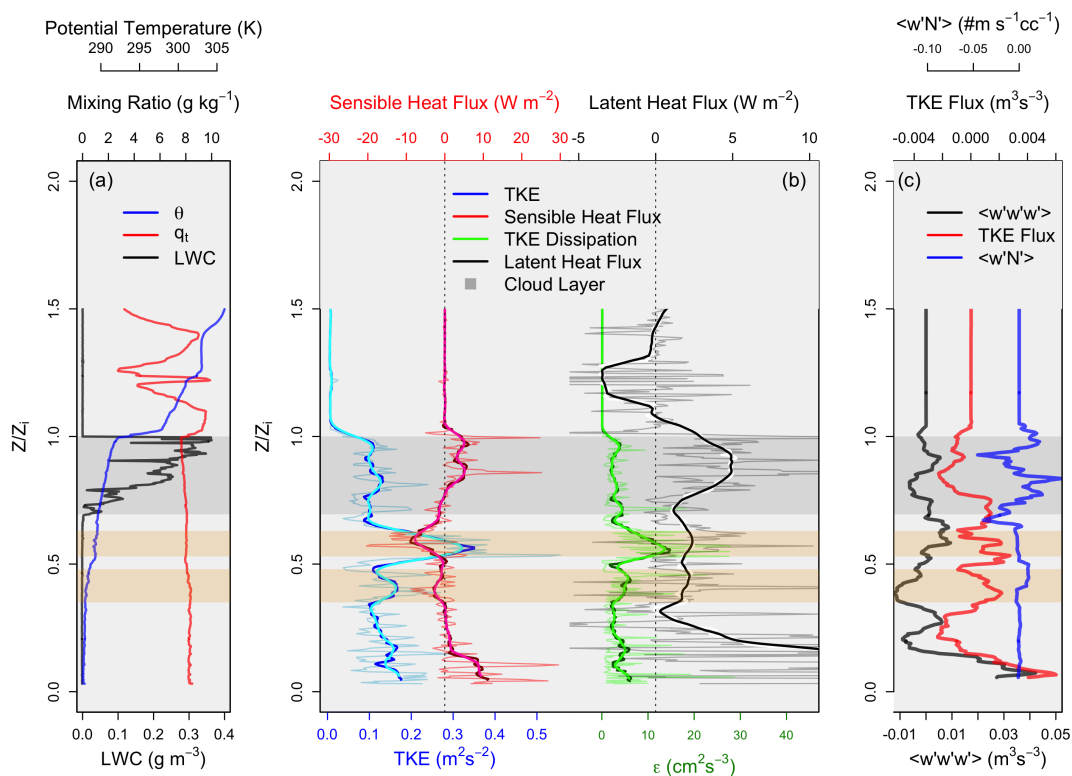
Figure 16. Vertical profiles as functions of normalized boundary layer height of (a) potential temperature (K) in blue, mixing ratio (g kg^{-1}) in red, and liquid water content (gm^{-3}) in black; (b) TKE (m^{2}s^{-2}) in blue, sensible heat flux (Wm^{-2}) in red, ϵ (cm^{2}s^{-3}) in green, and the latent heat flux (Wm^{-2}) in black. Note that the thin light colored lines represent raw values, while the dark thick lines represent smoothed averages; (c) $<w'w'w'>$ (m^{3}s^{-3}) in black, the TKE Flux (m^{3}s^{-3}) in red, and the droplet number concentration flux (m s^{-1}cc^{-1}) in blue. Note that the gray envelope represents the cloud layer, and the orange envelopes represent areas of interest (decoupling locations).
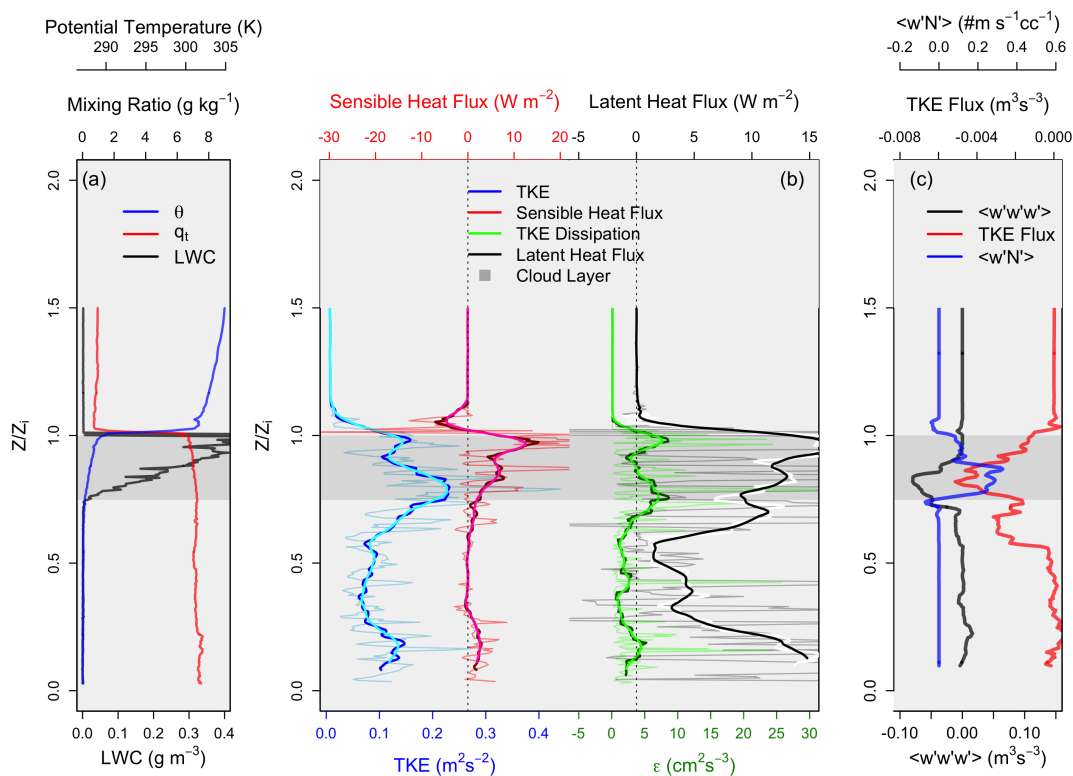
Figure 17. As in Figure 16, except for the well-mixed boundary layer case of RF03 (Oct 19th)

Table 1. Column (1): Research Flight (RF) identification; (2) The corresponding date; (3) Flight start and end times at Point Alpha. Note that local time: UTC – 4; (4) Boundary Layer conditions for each flight.

Flight	Date	Time (UTC)	BL Conditions
RF 3	Oct 19, 2008	12:05 - 14:40	Well Mixed
RF 4	Oct 21, 2008	12:10 - 14:50	Well Mixed
RF 5	Oct 22, 2008	12:00 - 14:40	Well Mixed
RF 7	Oct 26, 2008	12:00 - 15:00	Well Mixed
RF 8	Oct 27, 2008	15:55 - 19:00	Well Mixed
RF 9	Oct 29, 2008	11:50 - 15:00	Well Mixed
RF 10	Oct 30, 2008	11:50 - 15:00	Well Mixed
RF 11	Nov 01, 2008	12:05 - 15:05	Wind Shear / Moisture Above
RF 12	Nov 02, 2008	11:55 - 15:00	Moisture Above
RF 13	Nov 04, 2008	11:50 - 14:40	Wind Shear
RF 15	Nov 08, 2008	11:50 - 15:00	Decoupled
RF 16	Nov 09, 2008	11:50 - 15:05	Well Mixed
RF 17	Nov 10, 2008	14:45 - 18:00	Well Mixed
RF 18	Nov 12, 2008	11:50 - 15:15	Well Mixed

Table 2. Mean, standard deviation, and range of values for select variables over the 14 flights analyzed, with standard deviation values in parenthesis.

	Mean	Range
Boundary Layer Height (m)	1173 (119)	993 - 1450
Cloud Base (m)	936 (141)	716 - 1291
Cloud Thickness (m)	237 (101)	107 - 475
Boundary Layer Potential Temperature (K)	289 (1.12)	287 - 291
Boundary Layer Mixing Ratio (g kg^{-1})	7.51 (0.48)	6.83 - 8.32
Change in Potential Temperature (K)	16.8 (1.10)	13.89 - 18.42
Change in Mixing Ratio (g kg^{-1})	-5.53 (1.50)	-7.10 - 1.46
Boundary Layer PCASP (cc^{-1})	410 (127)	642 - 230
CDNC (cc^{-1})	262 (110)	80.5 - 423
Drop Size (μm)	12.33 (2.83)	9.6 - 20.5
Boundary Layer Wind Speed (m s^{-1})	4.42 (1.44)	2.03 - 6.31
Boundary Layer Wind Direction (°)	170 (46)	NA
Free Atmosphere Wind Speed (m s^{-1})	5.16 (1.89)	2.83 - 8.34
Free Atmosphere Wind Direction (°)	280 (115)	NA
α_θ	0.15 (0.08)	0.05 - 0.37
α_q	0.071 (0.049)	0.002 - 1.94

Table 3. Mean and range of values for select surface variables over the 14 flights analyzed, with standard deviation and the research flight number in parentheses for column mean and range, respectively.

	Mean	Range
Latent heat flux (Wm^{-2})	32.6 (11.5)	24.1 (RF 03) - 53.3 (RF 04)
Sensible heat flux (Wm^{-2})	8.6 (3.2)	3.93 (RF 03) - 17.1 (RF 01)
Bowen ratio	0.29 (0.15)	0.15 (RF 04) - 0.68 (RF 11)
Friction velocity (ms^{-1})	0.17 (0.023)	0.13 (RF 11) - 0.22 (RF12)
Vertical velocity variance (ms^{-1})	0.097 (0.017)	0.073 (RF 11) - 0.114 (RF 12)
TKE (m^{2}s^{-2})	0.14 (0.27)	0.051 (RF 11) - 0.20 (RF 12)
TKE dissipation rate (cm^{2}s^{-3})	5.14 (1.64)	9.40 (RF 11) - 2.64 (RF 12)

Table 4. Correlation coefficient values in the right-panel, with the variables in the left panel. Note that ↔ divides the variables being compared. GPH is geopotential height and BLH is boundary layer height. N_a and N_D represent the aerosol number concentration and the cloud droplet number concentration, respectively.

	Correlation
BLH ↔ GPH	-0.37
Wind speed ↔ GPH	0.14
Entrainment zone thickness ↔ GPH	0.22
in-cloud ϵ ↔ GPH	0.24
below cloud ϵ ↔ GPH	-0.15
in-cloud TKE ↔ GPH	0.23
below-cloud TKE ↔ GPH	-0.19
in-cloud sensible heat flux ↔ GPH	0.56
below-cloud sensible heat flux ↔ GPH	0.49
in-cloud latent heat flux ↔ GPH	0.29
below-cloud latent heat flux ↔ GPH	0.22
in-cloud ϵ ↔ BLH	-0.34
below-cloud ϵ ↔ BLH	-0.13
in-cloud TKE ↔ BLH	-0.32
below-cloud TKE ↔ BLH	-0.20
Sensible heat flux ↔ BLH	0.36
Wind speed ↔ sensible heat flux	0.64
Wind speed ↔ BLH	0.30
N_a ↔ TKE	0.35
N_D ↔ TKE	0.42
drop size (μm) ↔ TKE	-0.32
N_a ↔ ϵ	0.37
N_D ↔ ϵ	0.37
drop size (μm) ↔ ϵ	-0.32

Table 5. Mean values for each layer discussed in Figure 15, where the top rows represent data calculated using flight vertical profiles, while the bottom rows represent data calculated using horizontal flight legs. See the text for exact partitioning of the cloud layer.

Vertical Profile Data	$<w'\theta_v'>$ (Wm^{-2})	$<w'q'>$ (Wm^{-2})	TKE (m^{2}s^{-2})	ϵ (cm^{2}s^{-3})
Below Cloud	1.95	7.83	0.129	3.43
Cloud Base	3.75	4.88	0.165	4.69
Bottom Middle	12.21	8.18	0.178	4.37
Top Middle	13.58	13.77	0.167	4.73
Cloud Top	10.57	21.05	0.154	5.03
Horizontal Leg Data				
Below Cloud	6.13	17.67	0.136	4.16
Cloud Base	4.55	4.50	0.131	3.81
Bottom Middle	6.10	5.03	0.139	4.10
Top Middle	8.30	7.56	0.145	4.30
Cloud Top	4.10	6.02	0.108	3.01